# Effect of Synchronous Atmospheric Correction on the Accuracy of High-Resolution Remote Sensing Indices Images

Lingling Xu ⓘ, Wei Xiong ⓘ, Weining Yi, Wenyu Cui ⓘ, Xiao Liu, and Yuyao Wang

*Abstract*—**Accurate inversion of remote sensing indices images with high-resolution is an important basis for extracting the surface information on fine scale and the remote sensing application with high precision. Under the background that the effect of atmospheric correction on the inversion accuracy of medium-resolution remote sensing indices has been widely concerned, the atmospheric correction method based on the synchronous atmospheric parameters retrieved from the synchronization monitoring atmospheric corrector, which is on board the high-resolution multimode integrated imaging satellite (Gao Fen Duo Mo,) platform, is proposed. The "spaceborne—airborne" synchronous imaging experiment was conducted to investigate the effect of synchronous atmospheric correction on the accuracy of high-resolution remote sensing indices images. The low-altitude synchronous remote sensing indices images were taken as the reference standard, the correlation between the normalized difference vegetation index (NDVI) and normalized difference water index (NDWI) images after synchronous atmospheric correction and the reference images are improved by 4.27% and 12.22%, respectively. The mean errors in average NDVI and NDWI value of sampling plot decreased by 0.2489 and 0.1032, respectively. The average errors in the peak value of change rate of pixel index value are reduced by 0.1194 and 0.2288 in the case of NDVI and NDWI, respectively. Compared with the results of FLAASH, the synchronous atmospheric correction method shows better performance, especially in the targets with low reflectance (the atmospheric radiation contribution is higher than the surface radiation contribution), and in the adjacent area between two different ground objects. The results demonstrate that synchronous atmospheric correction can effectively improve the inversion accuracy of high-resolution remote sensing indices images and its ability of quantitative application.**

*Index Terms*—**Gao Fen Duo Mo (GFDM), high-spatial resolution, remote sensing indices image, synchronous atmospheric correction.**

Lingling Xu and Yuyao Wang are with the University of Science and Technology of China, Hefei 230026, China, and also with the Hefei Institutes of Physical Science, Chinese Academy of Sciences, Hefei 230031, China (e-mail: xll0507@mail.ustc.edu.cn; wangyuyao@mail.ustc.edu.cn).

Wei Xiong is with the Hefei Institutes of Physical Science, Chinese Academy of Sciences, Hefei 230031, China (e-mail: frank@aiofm.ac.cn).

Weining Yi, Wenyu Cui, and Xiao Liu are with the Hefei Institutes of Physical Science, Chinese Academy of Sciences, Hefei 230031, China, and also with the Key Laboratory of Optical Calibration and Characterization, Chinese Academy of Sciences, Hefei 230031, China (e-mail: yiwn@aiofm.cas.cn; cuiwenyu@aiofm.ac.cn; liux@aiofm.ac.cn).

## I. INTRODUCTION

A S AN important way to obtain geographic information, remote sensing technology has been widely used due to its rapid, accurate, economical, and periodic observation. The premise of the application of remote sensing technology is to extract the geographic information of interest, which is used to analyze the features of ground objects. The quantitative perception of geographic information, such as qualitative evaluation of green vegetation conditions [1], [2], [3], [4], [5], land cover classification and its change [6], [7], [8], [9], and geological hazards monitoring are based on remote sensing indices [10], [11].

Remote sensing indices are values that can be calculated based on remote sensing data and are often used to reflect the features of land cover [2], [7]. In related studies, the calculation of indices are predominantly based on surface reflectance [12], [13], [14]. The creation principle of remote sensing indices is to calculate the difference or ratio by combining different bands in multispectral or hyperspectral data. This approach serves to accentuate the target features within the index image while attenuating other background features [2], [14]. The surface reflectance used for the calculation of indices is affected by many factors, mainly from two aspects: 1) The influence of the remote sensor itself, such as the spectral response difference of different bands and the optical system error [16]; 2) Atmospheric interference, including the difference of atmospheric attenuation and path radiation in each band, and the cross-radiation interference of adjacent pixels [17], [18]. Radiation calibration can effectively suppress the influence of the former, and the uncertainty of calibration accuracy of on-orbit absolute radiation calibration is approximately 2%–5% [19], [20]. The error caused by atmospheric effects can be eliminated by atmospheric correction (AC) to enhance the quality of remote sensing images and ensure the accuracy of surface reflectance.

To improve the quality of information of interest extracted from remote measurements and its application, the impact of atmospheric conditions on remote sensing indices and the role of atmospheric corrections in improving the accuracy of remote sensing indices inversion have been investigated and evaluated. The quality of information extracted from remote measurements (e.g., vegetation indices) can be affected by atmospheric effects, which are the result of molecular scattering and absorption [21]. Errors caused by atmospheric effects can increase uncertainty

by up to 10%, depending on the spectral channel [22]. It is widely acknowledged that atmospheric effects typically result in a reduction in NDVI values [23], [24], [25] and also have an impact on the dynamic range of NDVI values [26]. In the case of the widely used Landsat imagery, it was found that atmospheric correction resulted in an increase of at least 0.05 in NDVI in desert, grassland, and woodland regions [27]. Moravec et al. [16] found that atmospheric correction can enhance NDVI by about 0.2 compared to the precorrection value, resulting in a relative difference in NDVI of 81%. Furthermore, the atmospheric correction of NDVI has a considerable effect on the estimation of land surface temperature (LST) in Landsat 8 image. Notably, the LST obtained by the 6S and FLAASH algorithms demonstrates enhanced accuracy across all study regions. In particular, the root mean square error (RMSE) of LST was significantly reduced from 1.624 in the uncorrected state to 0.3211 in the corrected state using the 6S algorithm [28]. Jiao et al. [29] introduced the atmospheric water vapor correction into the vegetation moisture index for the estimation of the canopy water content in vegetation. Based on the experimental results of Hyperion and GF5 satellite data, it was found that the corrected moisture index had a better RMSE for the canopy water content estimation, with an average reduction in RMSE of 3.47 mg/cm$^2$. The application of atmospheric correction on FY - 3A image using FLAASH has been shown has been shown to result in an increase of 35% in NDVI and a decrease of 8.7% in NDWI [29].

The use of high-resolution remote sensing images allows for the observation of finer surface features. With the increase in remote sensing imaging resolution, the research related the development and improvement of high-resolution remote sensing indices, as well as the extraction and application of surface detail information, have gained attention in recent years. Ma et al. [31] proposed morphological attribute building indices and shadow indices for high-resolution satellite data, which can effectively extract building features with high local contrast, internal homogeneity, shape and size of building features. Zhang et al. [32] proposed new vegetation index algorithms for hyperspectral data, such as the full-spectrum vegetation index (VIUPD). The index calculation utilizes the effective information of the entire band, thereby enhancing the ability to discern subtle changes in vegetation. Chen et al. [33] proposed inequality constraints and physical magnitude constraints to improve the method of extracting water bodies based on the traditional NDWI and MNDWI, which proved instrumental in the effective extraction of open waters in urban environments of high-spatial-resolution remote sensing images. Avdan et al. [34] concluded that the NDWI computed based on the RapidEy (5 m resolution) data demonstrated superior performance in extracting small water bodies and assessing water quality. Huang and Zhang [35] proposed a novel morphological building index (MBI) for the automated extraction of building from high-resolution remote sensing images. In comparison with the widely used object-based methods, the MBI is superior in terms of accuracy and visual detection. The mixed pixel effect in high-resolution images is relatively minimal, and it is expected that remote sensing information can more accurately reflect the actual features and their distribution. At least in theory, the atmospheric correction

of high-resolution remote sensing images is of considerable importance in improving the accuracy of remote sensing indices.

The atmosphere represents the primary source of noise for optical remote sensing, and it is of great importance to correct for atmospheric effects in order to obtain accurate surface reflectance. At present, two types of correction algorithms are primarily employed to eliminate the atmospheric influence and obtain the actual reflectance of the surface. The first type of algorithm is image-based, which mainly utilize the image's own features to perform atmospheric correction [36], [37], [38]. The typical methods include the dark pixel method, the histogram matching method, and the invariant target method, etc. The other one is the correction algorithm based on the radiative transfer model, and the commonly used radiative transfer models include 6S, LOWTRAN, and MODTRAN [39], [40], [41]. This class of methods is founded upon atmospheric models and atmospheric parameters to calculate the atmospheric radiation contribution, and subsequently subtract the atmospheric interference from the radiation received by the remote sensors to achieve the desired correction. Consequently, atmospheric data, which are measured in situ at the time of satellite imaging, are acquired to achieve optimal correction [42]. It has been demonstrated that methods based on radiative transfer modelling can facilitate more precise conversion of remote sensing data to surface reflectance [43], [44]. Nevertheless, in situ measured atmospheric data are rarely available, which limits the performance of atmospheric correction methods based on radiative transfer model.

The results of the above analysis of the differences in the medium-resolution remote sensing index before and after atmospheric correction indicate that atmospheric correction will result in a change to the value of remote sensing index. It is therefore believed that the remote sensing index will be improved, given that the atmospheric correction will enhance the accuracy of the surface radiation. Nevertheless, there is a notable absence of experimental validation demonstrating the impact of atmospheric correction on index error. Meanwhile, there is a lack of comprehensive analysis and experiments to evaluate the accuracy of indices based on indices images, including the accuracy of their spatial distribution. Moreover, few studies related to the atmospheric correction of high-resolution remote sensing images have conducted analyses or experiments to assess the impact of remote sensing index accuracy. Due to the spatial and temporal variability of atmospheric conditions, as well as the high heterogeneity of ground object features and the adjacent effect in the context of high-resolution conditions, it is of great importance to obtain synchronous atmospheric parameters, such as aerosol optical depth (AOD) and water vapor content (CWV), for the atmospheric correction of high-resolution optical remote sensing image [29], [45]. In addition, due to the high-frequency variation characteristics of feature distribution under high-resolution imaging conditions and the influence of adjacent effect, it is insufficient to evaluate the indices accuracy solely based on the numerical error of indices at typical feature sampling points. A more meaningful approach would be to compare the overall and detailed differences between the remote sensing indices images before and after the correction and the

simultaneous equivalent zero-visibility indices images of the ground surface.

In conclusion, high-resolution remote sensing images are of great significance for the accurate acquisition of surface information, and the high-precision remote sensing index inversion is its crucial foundation. The correction method based on synchronous atmospheric parameters can be effective in improving the accuracy of surface radiation. However, further investigation is required to ascertain its impact on the numerical precision of high-resolution remote sensing indices, its influence on the remote sensing indices images in the context of surface spatial heterogeneity, and its performance in comparison to existing classical atmospheric correction techniques. The findings of this study have the potential to provide technical references and methodological approaches for strategies to further enhance the quantitative level and application effectiveness of high-resolution remote sensing image information.

On 3 July 2020, the high-resolution multimode integrated imaging (Gao Fen Duo Mo, GFDM) satellite was successfully launched [48]. To obtain satellite data with high precision, the GFDM platform was configured with a synchronization monitoring atmospheric corrector (SMAC) [49]. As the first commercial atmospheric corrector with the capacity for polarization detection, SMAC is capable of acquiring field-of-view overlapped and time-synchronized atmospheric information [48], [49]. A synchronous atmospheric correction (Syn-AC) method is proposed based on the atmospheric parameters retrieved from SMAC. In the study, a "spaceborne—airborne" synchronous imaging experiment was designed and implemented for the purpose of evaluating the Syn-AC method on the inversion accuracy of remote sensing indices. The indices images retrieved from the low-altitude hyperspectral image were used as the reference images, and the errors in the indices results before and after synchronous atmospheric correction were analyzed. Additionally, the performance of the synchronous atmospheric correction method in comparison to other classical AC methods was evaluated. The analysis includes an overall difference analysis between the satellite-derived indices image and the reference indices image, an examination of the errors in the average indices value of the typical region within the satellite-derived indices images, and an investigation into the spatial variation trend of indices value of pixel at the junction area of different ground objects. Based on the above analysis, the impact of the synchronous atmospheric correction, which includes the correction of adjacent effect, on the accuracy of high-resolution remote sensing index images was investigated. Furthermore, the contribution of the research findings to the advancement of remote sensing information extraction and its practical applications was evaluated in the conclusion.

## II. STUDY AREA AND DATA

### A. Study Area

In the article, the accuracy of remote sensing indices, NDVI and NDWI, retrieved from high-spatial resolution remote sensing images before and after synchronous atmospheric correction was investigated and compared. As commonly used remote sensing indices, the two indices are representative. Studies have demonstrated that NDVI is effective to differentiate dense forest, non-forest and agricultural fields and to estimate various vegetation properties, including the LAI, biomass, plant productivity [5], [6], [7]. NDWI is mainly used for watershed analysis, e.g., spatial distribution and temporal variation of surface water bodies [33]. The bands involved in the calculation of NDVI and NDWI are also used to further calculate other indices, such as soil adjusted vegetation index, CI $_{green}$ (green chlorophyll index), and salinity indices, etc. [2], [5], [14]. To a certain extent, NDVI and NDWI can reflect the impact of synchronous atmospheric correction on the inversion accuracy in remote sensing indices, as well as the impact on the extraction and application of remote sensing information.

Fig. 1 illustrates the location of the study area. The study area is located on Dongpu Island, Hefei City of Anhui Province, China. The area comprises vegetation, water bodies, and artificial surfaces. To evaluate the NDVI results, a number of plots with different coverings, such as bare soil, asphalt, pavement, grassland, and green vegetation, were sampled. In order to evaluate the NDWI, different water bodies were selected for sampling. As shown in Fig. 1, the plots designated by red triangles are those utilized for the assessment of NDVI, while those labeled by yellow squares are intended for the evaluation of NDWI. It is noted that the sampling plots are also labeled with numbers in Fig. 1. The yellow numbers (1–25) and red numbers (1–9) are arranged in accordance with the mean NDVI and mean NDWI values of the labeled plots, respectively, and the indices values were retrieved from unmanned aerial vehicle (UAV) data. Table I contains the description of the sampling plots.

### B. Data

The data employed in the experiments contain three parts: synchronous atmospheric parameters, a multispectral image of GFDM satellite, and a low-altitude hyperspectral image. The synchronous atmospheric parameters are used for the correction of satellite image, and the satellite image is served as the data source to retrieve NDVI and NDWI images. While the NDVI and NDWI images retrieved from the UAV hyperspectral image are used as reference indices images, and a comparison is made between the satellite-derived results and these.

*1) Satellite Data:* On 3 July 2020, the GFDM satellite was launched, and a submeter-scale spatial resolution optical camera, SMAC, and other instruments were mounted on the satellite platform. As shown in Fig. 2(a), the main sensor is configured with eight multispectral bands and one panchromatic band with a spatial resolution of 2 and 0.5 m, respectively. In the experiment, the cloud-free multispectral satellite image of the study area was acquired and severed as the data source. Table II presents the observation parameters of the GFDM multispectral image.

An illustration of the SMAC equipment is given in Fig. 2(b). As the first commercial atmospheric corrector with the capacity of polarization detection, SMAC can obtain polarized and multispectral intensity information, which can be used for the retrieval of atmospheric parameters that are field-of-view overlapped and time-synchronized with the main optical sensor. SMAC covers
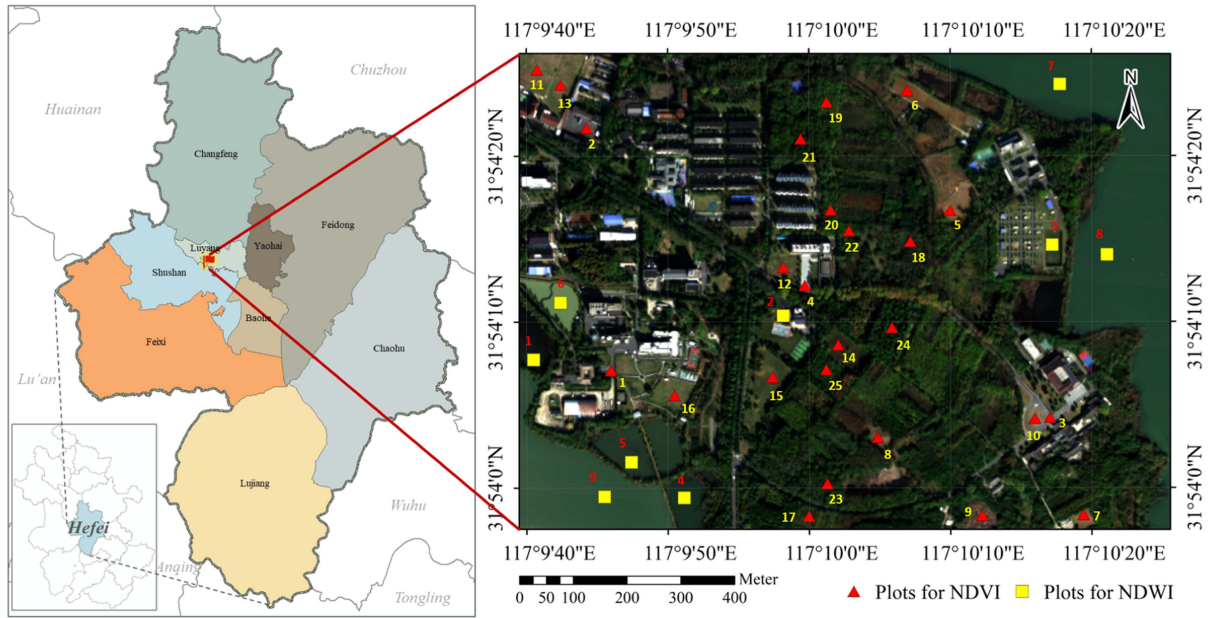
Fig. 1.    Location of study area and sampling plots. Plots for NDVI and NDWI are distinguished by labels.

TABLE I
DESCRIPTION OF THE SAMPLING PLOTS

| NDVI | | | NDWI | | |
|---|---|---|---|---|---|
| Number | Plot name | Description | Number | Plot name | Description |
| 1 ~ 4 | Artificial surface | Asphalt, pavement | 1 | Water body | With aquatic plant |
| 5 ~ 10 | Bare soil | No or little vegetation | 2 | Water body | With aquatic plant |
| 11 ~ 16 | Grassland | Grass field | 3 ~ 6 | Water body | Muddy water body |
| 17 ~ 25 | Vegetation | Tree | 7 ~ 9 | Water body | Clean water body |
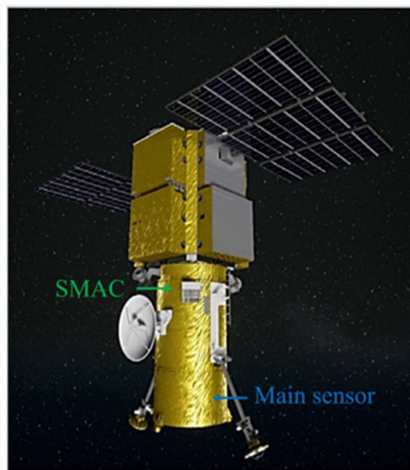


(a)
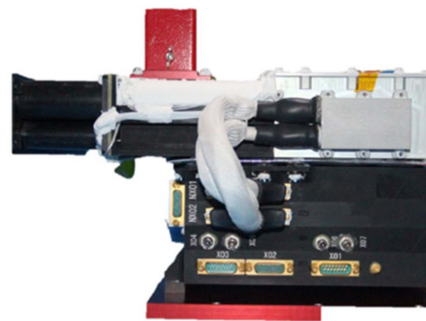


(b)

Fig. 2.    (a) GFDM satellite. (b) SMAC device [45].

eight wavelength bands, centered at 490(P), 550, 670(P), 870(P), 910, 1380, 1610(P), and 2250(P) nm, and polarization detection is available in channels denoted by "P" in parentheses. The spatial resolution of SMAC is approximately 6.7 km. Primarily designed for the aerosol detection within the atmospheric window, spanning from 490 to 2250 nm, SMAC also utilizes the 910 nm wavelength band to detect water vapor. As demonstrated by the studies of Li et al. [45], the synchronous atmospheric parameters, AOD (550 nm) and CWV, obtained from SMAC, were consistent with the ground measurements. In the study, the

TABLE II
OBSERVATION PARAMETERS OF GFDM SATELLITE MULTISPECTRAL IMAGE

| Data Level | Level 1A | Spatial resolution | 2m |
|---|---|---|---|
| Band/nm | B1: 450 ~ 520(Blue), B2: 520 ~ 590(Green), B3: 630 ~ 690(Red), B4: 770 ~ 890(NIR) | | |
| Imaging Time (UTC) | 2023-11-18 2:41:08 | Image Center | 31.95°N, 117.23°E |
| Solar Zenith | 54.12° | Satellite Zenith | 31.76° |
| Solar Azimuth | 158.02° | Satellite Azimuth | 96.61° |

TABLE III
PARAMETERS OF UAV-BORNE IMAGING SYSTEM

| | Parameters | Value |
|---|---|---|
| Flight parameters | Height | 200 m |
| | Moving speed | 8m/s |
| | Side overlap | 40% |
| Sensor parameters | Imaging mode | External push broom |
| | FOV | 25.36° |
| | Observation angle | Vertical downward |
| | Spectral Region(nm) | 400 ~ 1000 nm |
| | Spectral resolution | 2.5 nm |
| | Spatial resolution | 0.2 m |
| | Lens | 25 mm |
| | Band number | 241 |
| | Spectral channel number | 480(4X) |
| | Pixel value | Ground reflectance |

atmospheric parameters were acquired from SMAC and used as input for Syn-AC method, and the values are 0.64 g/cm$^2$ and 0.173 for CWV and AOD (550 nm), respectively.

*2) UAV-Borne Data:* The implementation of the "spaceborne—airborne" experiment involved the collection of a near-surface hyperspectral image using a UAV-borne hyperspectral imaging system (ZK-VNIR-FPG480L, Zhike). The system, developed by Yuanda Data Technology (Beijing, China), comprises a hyperspectral imager (ZK-VNIR-FPG480L) and a six-rotor UAV manufactured by the Da Jiang Company (Shenzhen, China). The influence of atmospheric interference on the low-altitude image is so weak that it can be ignored. Therefore, the remote sensing indices results retrieved from the low-altitude image can be used as a reference for experimental comparison. In the experiment, the UAV flight mission was taken on a cloudless day which the satellite overpassed (18 November 2023), and the hyperspectral data with a spatial resolution of 0.2 m was acquired. The parameters of the UAV-borne imaging system are listed in Table III.

## III. METHODOLOGY

### A. Synchronous Atmospheric Correction Method

The accuracy of remote sensing indices images is significantly influenced by atmospheric correction. Based on the retrieval of SMAC, a synchronous atmospheric correction method was proposed. As illustrated in Fig. 3, the method consists of processing raw data from SMAC, inversion of atmospheric parameters, and atmospheric correction on GFDM image.
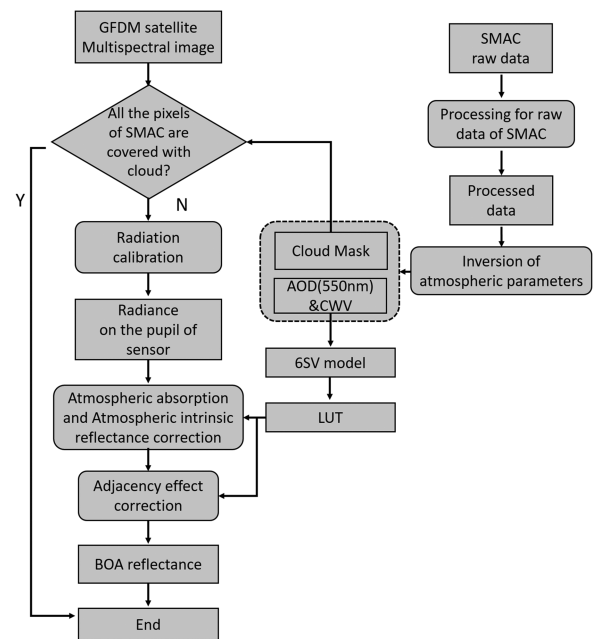


Fig. 3.    Flowchart of synchronous atmospheric correction method.

*1) Processing for Raw Data of SMAC:* The raw data of SMAC is constituted of digital number (DN). In order to perform the inversion of synchronous atmospheric parameters, the polarization data and the radiation data of SMAC are required as input. Consequently, the raw data of SMAC must be processed before the inversion can be carried out. The processing procedure are consisted of six steps.

1) Data validation is conducted to ensure the data involved in the processing are valid.

2) According to the calibration configuration of SMAC, the effective signal is obtained by subtracting the dark current from the original DN values.

3) The spectral radiance of the nonpolarization detection bands (550, 910, and 1380 nm) is calculated, the formula is presented

$$L(\lambda) = \frac{\text{DN}_\lambda}{A_\lambda * Z_\lambda} \qquad (1)$$

where $Z_\lambda$ and $A_\lambda$ are the gain and absolute spectral response for the band $\lambda$, respectively. The unit of radiance $L(\lambda)$ is equal to $\mu W/cm^2/nm/sr$.

4) Considering the bands with polarization (490(P), 670(P), 870(P), 1610(P), and 2250(P) nm), the Stokes parameters $[I, Q, U]$ [51] are calculated

$$\begin{bmatrix} I_\lambda \\ Q_\lambda \\ U_\lambda \end{bmatrix} = \frac{1}{A_\lambda^2 * Z_\lambda^2} \begin{bmatrix} \text{DN}_\lambda^1/T_\lambda^1 \\ \text{DN}_\lambda^2 \\ \text{DN}_\lambda^3/T_\lambda^3 \end{bmatrix}$$

$$\bullet \begin{bmatrix} 1 & \cos\left(2\left(\alpha_\lambda + \alpha_\lambda^1\right)\right) & -\sin\left(2\left(\alpha_\lambda + \alpha_\lambda^1\right)\right) \\ 1 & \cos\left(2(\alpha_\lambda + \alpha_\lambda^2)\right) & -\sin\left(2(\alpha_\lambda + \alpha_\lambda^2)\right) \\ 1 & \cos\left(2(\alpha_\lambda + \alpha_\lambda^3)\right) & -\sin\left(2(\alpha_\lambda + \alpha_\lambda^3)\right) \end{bmatrix}^{-1} \qquad (2)$$

where $\lambda$ and $i$ are the band and channel, respectively. $\text{DN}_\lambda^i$ refers to the digital number, $\alpha_\lambda^i$ denotes the polarization orientation angle, and $T_\lambda^i$ represents the relative transmittance.

5) The observation parameters of SMAC, including viewing zenith and azimuth angles, solar zenith and azimuth angles, and central longitude and latitude, are inferred from the auxiliary packets of main sensor.

6) Above all, the data generated in steps (1) to (5) are packaged in a certain format and used for atmospheric parameters inversion.

*2) Inversion of Atmospheric Parameters:*

*a) Cloud mask:* The existence of clouds causes radiance interference to inversion of atmospheric parameter [45]. Consequently, it is essential to identify and remove cloud-covered pixels of SMAC prior to the inversion. In the present study, a threshold-based judgment method has been employed for the identification of cloud-covered pixels of SMAC.

First, the reflectance at the top of the atmosphere at 490 nm ($\rho_{490}^{\text{TOA}}$) was calculated and used for detecting whether the pixel of SMAC was contaminated by thick cloud [52]. Then, cirrus clouds can be identified based on $\rho_{1380}^{\text{TOA}}$ [52]. Furthermore, based on the mask result, normalized difference dust indices (NDDI) was calculated to detect cloud-contaminated pixels over desert [53], and normalized difference snow indices (NDSI) was used in the case of pixels on snow [54]. For each pixel of SMAC, the following were calculated, and the pixel was identified as being contaminated when at least one of the following equations stands:

$$\rho_{490}^{\text{TOA}} > 0.4 \qquad (3)$$

$$\rho_{1380}^{\text{TOA}} > 0.0025 \qquad (4)$$

$$\text{NDDI} = \frac{\rho_{2250nm}^{\text{TOA}} - \rho_{490nm}^{\text{TOA}}}{\rho_{2250nm}^{\text{TOA}} + \rho_{490nm}^{\text{TOA}}} < 0 \qquad (5)$$

$$\text{NDSI} = \frac{\rho_{550nm}^{\text{TOA}} - \rho_{1610nm}^{\text{TOA}}}{\rho_{550nm}^{\text{TOA}} + \rho_{1610nm}^{\text{TOA}}} > 0.13. \qquad (6)$$

*b) Aerosol:* For simplicity, the simulated polarized TOA reflectance $\rho_{p,\lambda}^{\text{TOA}}$ can be represented as follows [55], [56]:

$$\rho_{p,\lambda}^{\text{TOA}}(\theta_s, \theta_v, \Delta\phi) = \rho_{p,\lambda}^{\text{Atm}}(\theta_s, \theta_v, \Delta\phi)$$
$$+ T_{p,\lambda}^\downarrow(\theta_s)\rho_p^{\text{Surf}}(\theta_s, \theta_v, \Delta\phi)T_{p,\lambda}^\uparrow(\theta_v) \quad (7)$$

where $\phi$, $\theta_s$, and $\theta_v$ correspond to relative azimuth angle, solar zenith, and viewing zenith angle for wavelength $\lambda$, respectively; $\rho_{p,\lambda}^{\text{Atm}}$ denotes the polarized scattering interference from molecules and aerosols; $\rho_p^{\text{Surf}}$ is the polarized reflectance of ground surface, and it is wavelength-independent [57]; and $T_{p,\lambda}^\downarrow$ $T_{p,\lambda}^\uparrow$ is the bidirectional total transmittance.

Considering different observation geometries ($\theta_s, \theta_v$, and $\phi$), atmospheric model, AOD, ground elevation, and other key conditions, a look-up table (LUT) has been constructed on the basis of the unified linearized vector radiative transfer model [58]. In addition, $\rho_{p,\lambda}^{\text{TOA}}$ could be calculated by the polarized radiance. Therefore, as long as $\rho_{p,\lambda}^{\text{Atm}}$ and simulated $\rho_{p,\lambda}^{\text{TOA}}$ could be obtained from the LUT, and surface-polarized reflectance $\rho_p^{\text{Surf}}$ was known, the optimal parameter combination related to AOD was retrieved as soon as the parameters corresponding to the smallest value function was obtained based on the optimal estimation theory [59], and the AOD can be retrieved, too.

*c) Water vapor:* Based on the assumption that the ground is Lambert surface, and the gaseous absorption contribution from scattering process cannot be ignored, the simulated scalar reflectance $\rho_\lambda^{\text{TOA}}$ can be presented as follows [60]:

$$\rho_\lambda^{\text{TOA}}(\theta_s, \theta_v, \Delta\phi) = T_g(\text{OG}) \bullet \left[ \rho_\lambda^{\text{Atm}}(\theta_s, \theta_v, \Delta\phi) \right.$$
$$\left. + \frac{T_\lambda^\downarrow(\theta_s)\rho_\lambda^{\text{Surf}}(\theta_s, \theta_v, \Delta\phi)T_\lambda^\uparrow(\theta_v)}{1 - S_\lambda\rho_\lambda^{\text{Surf}}(\theta_s, \theta_v, \Delta\phi)}T_g(\text{H}_2\text{O}) \right] \qquad (8)$$

where $\rho_\lambda^{\text{Atm}}$ denotes path reflectance contributed by molecules and aerosols, $\rho_\lambda^{\text{Surf}}$ denotes the surface reflectance, $T_g(\text{OG})$ and $T_g(\text{H}_2\text{O})$ denote the transmission by gases in atmosphere, $S_\lambda$ is the hemispherical albedo, and $T_\lambda(\theta_s)^\downarrow T_\lambda(\theta_s)^\uparrow$ symbolizes the total transmittance.

Assuming for the argument that the surface reflectance at VIS and NIR bands is similar, the water vapor absorption transmittance can be obtained by calculating the ratio of the water vapor absorption channel (910 nm) to the window channel (870 nm) [45]

$$\frac{\rho_{910}^{\text{TOA}} - \rho_{910}^{\text{Atm}}}{\rho_{870}^{\text{TOA}} - \rho_{870}^{\text{Atm}}} \cong \frac{T_{910}^\downarrow(\theta_s)T_{910}^\uparrow(\theta_v)}{T_{870}^\downarrow(\theta_s)T_{870}^\uparrow(\theta_v)} \equiv T. \qquad (9)$$

Then, the CWV was derived by an empirical formula as follows [61], [62]:

$$\text{CWV} = \frac{t_1 + t_2 \ln(T) + t_3 [\ln(T)]^2}{M} \quad (10)$$

where $M = 1/(\cos \theta_s) + 1/(\cos \theta_v)$, $t_1 = 0.1946$, $t_2 = 0.5202$,
and $t_3 = 28.11$ represent the fitting coefficients of empirical formula [45].

*3) Atmospheric Correction on GFDM Image:* In the context of high-resolution optical satellite remote sensing imagery, the primary objective of atmospheric correction is to eliminate the influence of atmospheric conditions and adjacent surfaces on the observed reflectance, thereby facilitating the accurate estimation of surface reflectance [47]. In this study, based on the atmospheric radiative transfer model and with the atmospheric parameters of SMAC as input, the multispectral image of GFDM satellite is corrected to obtain the corresponding BOA reflectance.

First, radiometric calibration is applied, and the top-of-atmosphere radiance is obtained

$$L = k \cdot DN + b \quad (11)$$

where $L$ represents the radiance (W $\cdot$ m$^{-2}$ $\cdot$ sr$^{-1}$ $\cdot$ $\mu$m$^{-1}$), and $k$ and $b$ denote the gain coefficient and the offset, respectively. Considering the Lambert surface assumption, the TOA radiance can also be represented as follows:

$$L = L_{\text{path}} + T(\theta_v) \frac{\rho^* E_g(0)}{\pi(1 - \rho^* S)} \quad (12)$$

where $L_{\text{path}}$ is the path radiance along the ground surface-to-sensor direction, and $\rho^*$ denotes the surface reflectance. $T(\theta_v)$ is the upwelling and downwelling transmittance factor; $E_g(0)$ denotes the solar irradiance; and $S$ denotes the atmospheric hemispheric albedo. With 6SV transfer model, an LUT has been constructed to cover different AOD and CWV based on the observation geometry, atmospheric model, ground elevation and other key conditions of the satellite image to be corrected. Then, the path radiance and transmittance corresponding to the AOD and CWV retrieved from SMAC could be obtained, and $L_{\text{path}}(\text{AOD}, \text{CWV})$ and $T(\theta_v, \text{AOD}, \text{CWV})$ are used to represent the two factors. Thus, the surface reflectance $\rho^*$, which contained the radiance contribution from neighbor pixels, can be expressed as follows:

$$\rho^* = \frac{L - L_{\text{path}}(\text{AOD}, \text{CWV})}{\frac{T(\theta_v, \text{AOD}, \text{CWV}) E_g}{\pi} + S(L - L_{\text{path}}(\text{AOD}, \text{CWV}))}. \quad (13)$$

Considering the adjacency effect, the average reflectance of neighboring pixels $\rho_{\text{Background}}$ can be represented as follows:

$$\rho_{\text{Background}} = \sum_m \sum_n \rho'(\gamma, \eta) \text{Weight}(\gamma, \eta, \theta_v) \quad (14)$$

where $\rho'(\gamma, \eta)$ denotes the pixel reflectance in row $\gamma$ and column $\eta$, and $\text{Weight}(\gamma, \eta, \theta_v)$ denotes the weight coefficient describing the contribution ratio of surrounding pixel. The magnitude of the weight coefficient is determined by the atmospheric state
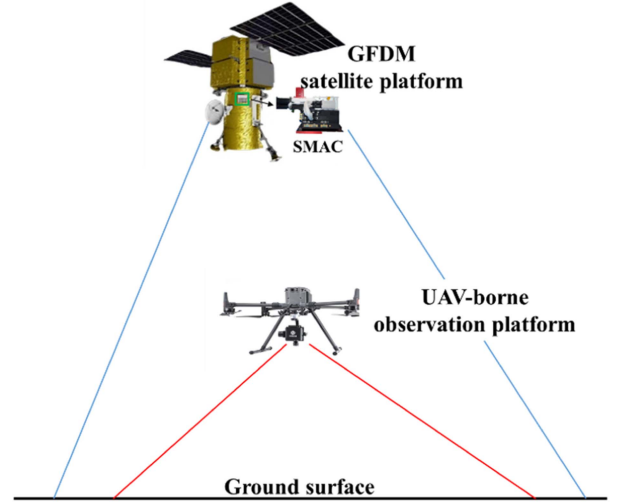


Fig. 4.   Schematic diagram of experiment system.

(mainly the aerosol optical depth), the spatial distance between the background and the target, and the reflectivity difference between them [47].

Subsequently, the interfering contribution of neighboring pixels is deducted from $\rho^*$ after correction of adjacency effect, and the reflectance product $\rho_t$ can be expressed as follows [46]:

$$\rho_t = \rho^* + q(\rho^* - \rho_{\text{Background}}) \quad (15)$$

where $q$ denotes the correction factor of adjacency effect. In this article, the ratio between diffuse transmittance and direct transmittance is used as the factor [46].

## B. Experimental Method

*1) Experiment System:* To compare the satellite-derived indices images with the indices images retrieved from UAV hyperspectral data, the "spaceborne—airborne" synchronous imaging experiment was proposed, on the basis of which the experiment system was constructed and an experiment flow was designed. In accordance with the features of synchronous measurement, the experiment system is constituted of two parts: the GFDM satellite platform and the UAV-borne observation system (see Fig. 4). The satellite platform is equipped with a high-resolution optical camera and an SMAC, while the UAV-borne observation platform is equipped with a hyperspectral imager. The main camera onboard the GFDM satellite and the UAV-borne camera observed the same area at the same time, and the images of the study area were acquired. Concurrently, as the satellite passed overhead, the SMAC collected atmospheric parameters precisely aligned with the satellite imagery in both space and time.

As shown in Fig. 5, the experiment flow contains two phases: 1) The retrieval of input data. First, the UAV-based data, GFDM satellite image and synchronous AOD (550 nm) and CWV were collected. Then, the processing of UAV-based data was conducted to obtain UAV-derived surface reflectance image. Subsequently, the radiation calibration of satellite image was
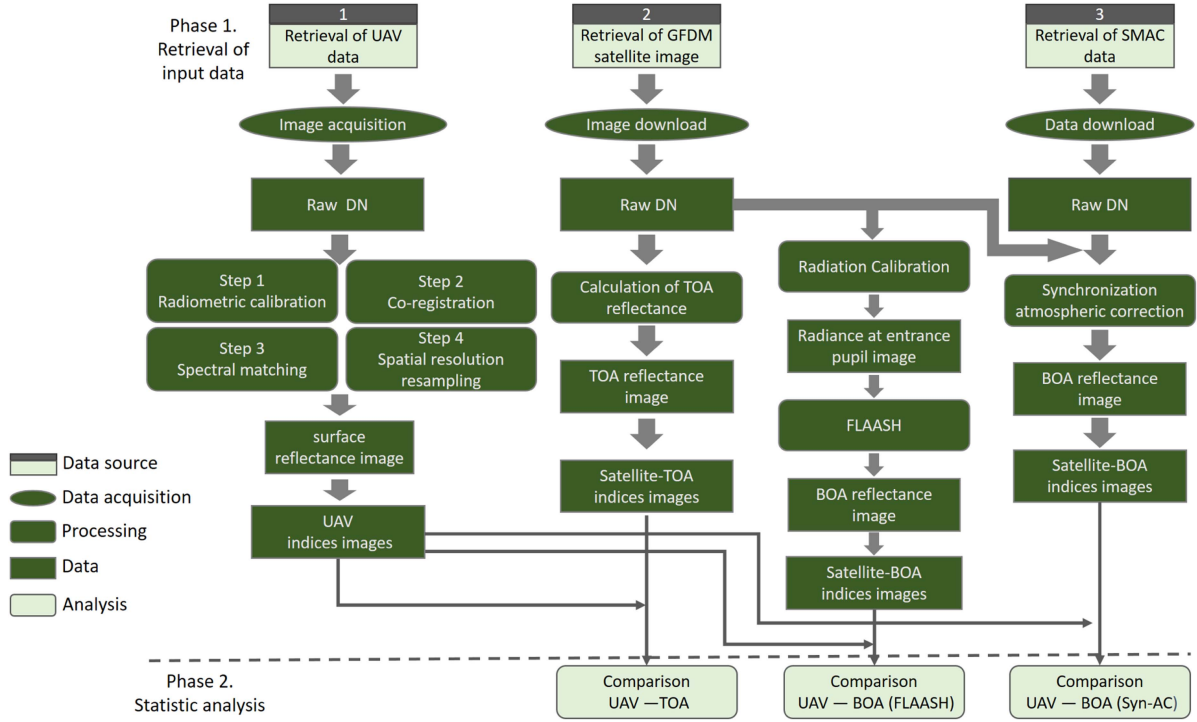
Fig. 5. Flowchart of experiment.

carried to obtain satellite TOA reflectance image, and FLAASH was applied on it to retrieve satellite BOA reflectance image. Additionally, Syn-AC method was applied on satellite image based on synchronous parameters to retrieve satellite BOA reflectance image, too. After the processing, the remote sensing indices images were retrieved from the UAV and satellite (TOA and BOA) reflectance images; 2) Statistical analysis. The analysis contains the comparisons between the indices images retrieved from the satellite TOA reflectance image and the BOA reflectance images obtained by Syn-AC and FLAASH with the UAV-derived indices images.

*2) Retrieval of Remote Sensing Indices Images:* In the study, the results of the comparison between the satellite-derived indices images and the UAV-derived truth were evaluated. Two kinds of classical indices were selected for calculation: NDVI, one of the most commonly used indices to identify vegetation and its health [63]; NDWI, frequently employed for highlighting water information in the optical satellite images [64]. The satellite-derived indices image was obtained by calculating the indices value of pixels in the satellite TOA and BOA reflectance images before and after atmospheric correction, and the pixel indices value $\text{NDVI}(i,j)_{\text{SAT}}$ and $\text{NDWI}(i,j)_{\text{SAT}}$ are calculated

$$\text{NDVI}(i,j)_{\text{SAT}} = \frac{\rho(i,j)_{B4} - \rho(i,j)_{B3}}{\rho(i,j)_{B4} + \rho(i,j)_{B3}} \quad (16)$$

$$\text{NDWI}(i,j)_{\text{SAT}} = \frac{\rho(i,j)_{B2} - \rho(i,j)_{B4}}{\rho(i,j)_{B2} + \rho(i,j)_{B4}} \quad (17)$$

where $\rho(i,j)_{B2}$, $\rho(i,j)_{B3}$ and $\rho(i,j)_{B4}$ are the reflectance at the green, red, and near-infrared bands in row $i$ and column $j$ of satellite image, respectively.

Subsequently, the UAV-derived indices image was extracted from the hyperspectral reflectance image. To obtain the surface reflectance with high precision, a series of processing steps were conducted on the raw UAV-borne hyperspectral data: radiometric correction, geometric registration, spectral matching and spatial resampling. First, the radiometric calibration was applied based on the DN of a gray-calibrated plane before and after each flight. Then, the geometric registration of the UAV-borne and satellite images was made based on the ground control points. Based on the UAV reflectance image after geometric registration, the spectrum of every pixel in the hyperspectral image was matched to the spectral response function of the GFDM satellite, and the corresponding band reflectance $\rho_{B_i}$ was obtained. So, an image comprising four bands (Blue: B1, Green: B2, Red: B3, NIR: B4) was yielded after the spectral matching

$$\rho_{B_i} = \frac{\int_{\lambda_i^1}^{\lambda_i^2} \rho(\lambda)\text{RSRR}(\lambda)d\lambda}{\int_{\lambda_i^1}^{\lambda_i^2} \text{RSRR}(\lambda)d\lambda} \quad (18)$$

where $\rho(\lambda)$ denotes the reflectance spectrum from the hyperspectral image, and $\text{RSRR}(\lambda)$ denotes the relative spectral radiative response of GFDM. $\lambda_i^1$ and $\lambda_i^2$ are the lower and upper limits of integration at the band $B_i(i=1,2,3,4)$, and the integration range of band $B_i$ refers to the band range of the satellite band $B_i$ in Table II.

Furthermore, in order to facilitate a direct comparison of the indices results at the same spatial resolution, the spatial resolution of all bands of the UAV image after spectral matching was resampled to 2 m, which is identical to the spatial resolution of the GFDM multispectral imagery. Ultimately, the UAV-borne

reflectance image with a spatial resolution of 2 m was acquired and served as a source to retrieve indices images. The pixel indices values, $\text{NDVI}(m,n)_{\text{UAV}}$ and $\text{NDWI}(m,n)_{\text{UAV}}$, were calculated

$$\text{NDVI}(m,n)_{\text{UAV}} = \frac{\rho(m,n)_{B4} - \rho(m,n)_{B3}}{\rho(m,n)_{B4} + \rho(m,n)_{B3}} \quad (19)$$

$$\text{NDWI}(m,n)_{\text{UAV}} = \frac{\rho(m,n)_{B2} - \rho(m,n)_{B4}}{\rho(m,n)_{B2} + \rho(m,n)_{B4}} \quad (20)$$

where $\rho(m,n)_{B2}$, $\rho(m,n)_{B3}$, and $\rho(m,n)_{B4}$ are reflectance at the green, red, and near-infrared bands in row $m$ and column $n$ of UAV reflectance image, respectively.

Therefore, following the aforementioned processing, the synchronous UAV-derived and satellite-derived remote sensing indices images, exhibiting a uniform spectral response and spatial resolution, were obtained through the calculation of pixel NDVI and NDWI values.

*3) Statistic Analysis:* In the study, the indices images retrieved from the low-altitude hyperspectral image were used as the reference images. The errors of the indices result before and after atmospheric correction were analyzed to investigate the performance of synchronous atmospheric correction in enhancing the inversion precision of remote sensing indices.

*a) Correlation between satellite-derived and UAV-derived indices images:* The satellite-derived and UAV-derived indices images are consistent in temporal and spatial scales. The difference between the indices images would reflect the comprehensive difference of indices results, including the difference in numerical and spatial distribution. So, the correlation between the indices image retrieved from the satellite TOA and BOA reflectance and that retrieved from UAV-based data were calculated and compared, and the calculation equation is as follows:

$$r = \frac{\sum_m \sum_n (A_{mn} - \overline{A})(B_{mn} - \overline{B})}{\sqrt{\left(\sum_m \sum_n (A_{mn} - \overline{A})^2\right)\left(\sum_m \sum_n (B_{mn} - \overline{B})^2\right)}} \quad (21)$$

where $A$ and $B$ represent satellite-derived and UAV-based indices images, respectively. $A_{mn}$ and $B_{mn}$ indicate the pixel indices values in row $m$ and column $n$, and $\overline{A}$ and $\overline{B}$ represent the mean indices values of all the pixels in indices image.

*b) Comparison of average indices value of typical region:* Moreover, a number of sampling plots within the satellite-derived indices image were selected, and the mean indices value of each sampling plot was calculated for comparison with the mean indices result of the corresponding plots in the UAV-derived image. The mean indices value of each sampling plot $P_k$ was calculated

$$\overline{\text{Value}}(P_k) = \frac{\sum_{i=1}^{n} \sum_{j=1}^{m} \text{Value}(i,j)}{m * n}, (i,j) \in P_k \quad (22)$$

where $m$ and $n$ denote the numbers of column and row of sampling plot $P_k$, respectively. The indices value of the pixel at row $i$ and column $j$ of $P_k$ is represented by $\text{Value}(i,j)$.

For the vegetation indices, the plots with different ground covers were selected, and the changes of average NDVI value

before and after AC of the plots were investigated. For the water indices, different water bodies were selected to test the changes of average NDWI value before and after AC. First, the absolute error ($E_A$) of the average indices result before and after AC with the UAV truth value was calculated to evaluate the difference between them. In addition, the RMSE between UAV-derived values and satellite-derived results was calculated, too. The formulas are as follows:

$$E_A(P_k) = |\overline{\text{Value}}(P_k)_{\text{SAT}} - \overline{\text{Value}}(P_k)_{\text{UAV}}| \quad (23)$$

$$X_{\text{RMSE}} = \sqrt{\frac{\sum_{k=1}^{N}(E_A(P_k))^2}{N}} \quad (24)$$

where $\overline{\text{Value}}(P_k)_{\text{SAT}}$ and $\overline{\text{Value}}(P_k)_{\text{UAV}}$ are the mean indices value of sampling plot $P_k$ in satellite-derived and UAV-derived indices images, respectively, and $N$ represents the number of sampling plots.

*c) Comparison of changes in pixel indices value:* In the process of optical remote sensing imaging, the radiation interference to the target pixels from the surrounding pixels occurs due to atmospheric scattering, which is known as the adjacency effect [47], [65]. As the contribution of adjacency effect, the edge of ground object is blurred and the contrast is reduced, which increases the uncertainty of classification when using these pixels for ground object recognition [65], [66]. Moreover, there may be a deviation between the calculated results and the real value when remote sensing data is used to acquire ground object information due to the different degrees of adjacency effect on each band. Studies have demonstrated that the adjacent effect must be considered when the spatial resolution of the sensor exceeds than 1 km [67].

In the study, as the "spaceborne–airborne" synchronous imaging experiment was implemented, the satellite multispectral image and UAV-borne image with a high spatial resolution of 2 and 0.2 m were collected and served as data sources. Furthermore, the atmospheric correction of satellite images by Syn-AC and FLAASH methods incorporates the adjacent effect correction. Consequently, the impact of adjacent effect correction on the inversion of remote sensing indices can be investigated by assessing the variation in the indices values of adjacent pixels at the boundary of two ground objects in the indices image. In the case of NDVI, eight regions were selected, and each region contains vegetation on the sides and the asphalt road/bare soil in the middle. The pixel value of the vegetation and nonvegetation were obtained from the satellite-derived NDVI images and compared with the true value of the UAV-NDVI. Meanwhile, six regions are selected for NDWI, and each region consists of two adjacent water bodies and the ground area between them. The NDWI values of the pixels within the adjacent water bodies and nonwater bodies are acquired and compared with the corresponding UAV-NDWI values. For the statistical analysis, the absolute errors of the pixel indices results before and after AC with the UAV truth values were calculated. Then, the change rate of pixel indices value was investigated by calculating the first derivative of the indices values of two adjacent pixels

$$E_A(x,y) = |\text{Value}(x,y)_{\text{Satellite}} - \text{Value}(x,y)_{\text{UAV}}| \quad (25)$$
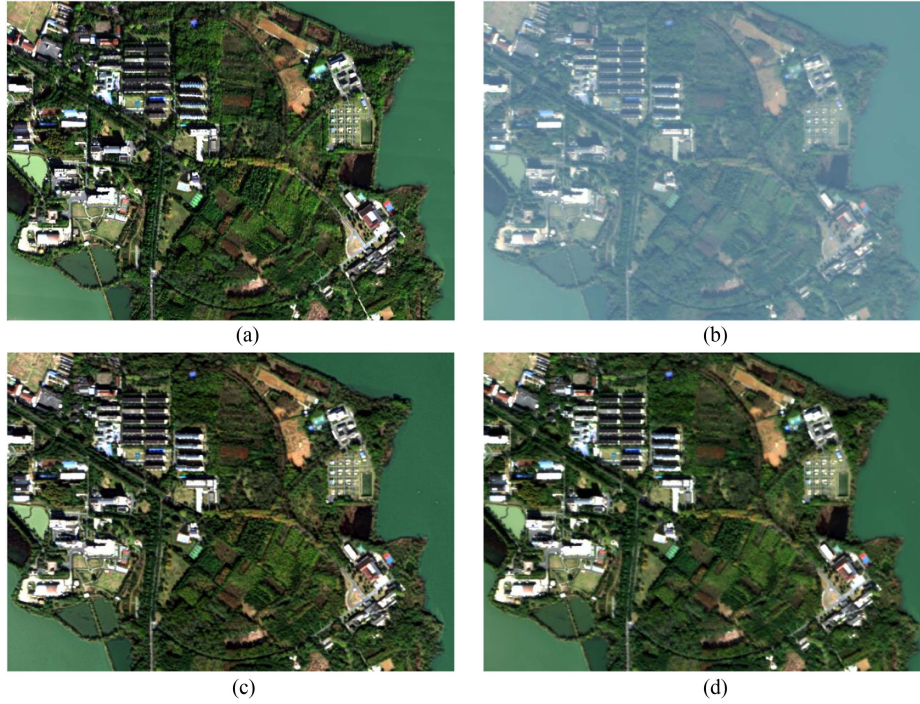
Fig. 6. RGB composition in true color of (a) UAV-borne image, (b) original satellite image, (c) satellite image corrected by Syn-AC, and (d) satellite image corrected by FLAASH.

$$\text{Rate}_X = \left| \frac{\text{Value}(x, y) - \text{Value}(x + \Delta x, y)}{\Delta x} \right| \quad (26)$$

$$\text{Rate}_Y = \left| \frac{\text{Value}(x, y) - \text{Value}(x, y + \Delta y)}{\Delta y} \right| \quad (27)$$

where $\text{Value}(x, y)_{\text{Satellite}}$ and $\text{Value}(x, y)_{\text{UAV}}$ are the indices values of pixels at row $i$ and column $j$ in the satellite-derived and UAV-derived indices images, respectively. $E_A(x, y)$ represents the absolute error in the pixel value. $\text{Rate}_X$ and $\text{Rate}_Y$ are the first derivative values of the indices value of two adjacent pixels along the $X$ and $Y$ direction, respectively. $\Delta x$ and $\Delta y$ denote the deviations along $X$ and $Y$ direction, respectively. In the study, the derivative of two adjacent pixels was evaluate, so both $\Delta x$ and $\Delta y$ equal one. It noted that both $\text{Rate}_X$ and $\text{Rate}_Y$ are hereinafter referred to as Rate.

Based on the results of the change rate of pixel indices value, the peak values of the change rate are mainly investigated. The absolute errors between the peak values of the change rate of the pixel values in the UAV-derived indices images and the corresponding satellite-derived results were calculated

$$E_A(\text{Rate}^P) = \left| \text{Rate}_{\text{SAT}}^P - \text{Rate}_{\text{UAV}}^P \right| \quad (28)$$

where $\text{Rate}_{\text{SAT}}^P$ and $\text{Rate}_{\text{UAV}}^P$ are the peak values of the change rate of indices value of pixels in the satellite-derived and UAV-derived indices images, respectively

*4) Comparison With FLAASH:* The fast line-of-sight atmospheric analysis of hypercubes (FLAASH) is a first-principle atmospheric correction tool based on the precalculated results from the MODTRAN 4.0 radiative transfer model [68]. The

tool is capable of correcting wavelengths within the visible, near-infrared, and shortwave infrared ranges up to 3 $\mu$m [69]. Independent of synchronously measured atmospheric parameters, atmospheric influence in FLAASH was estimated based on the horizontally homogenous and vertically stratified atmosphere models, which are constructed in accordance with built-in models in MODTRAN and climatology settings [69]. The issue of the adjacent effect is addressed in FLAASH [68]. In ENVI version 5.3, the input data for FLAASH is the TOA radiance, while the remaining settings are obtained from the metadata file of the satellite imagery to be corrected. In the experiment, the aerosol model was rural, and the atmospheric model was set up in accordance with the scene center location and imaging date. The altitude was set to 0.05 km according to the study locality. The input parameters remained consistent with those used in the Syn-AC method. FLAASH was applied to the multispectral image captured by the GFDM satellite, and the BOA reflectance was obtained to invert the spectral indices. Then, the indices results were also evaluated by comparing them with the UAV truth values, and the performance of FLAASH was compared with that of the synchronous atmospheric correction method.

## IV. RESULTS

### A. Atmospheric Correction Result

Fig. 6 illustrates the RGB composition in true color (Band1: blue, Band2: green, Band3: red) of the original and corrected satellite images, and UAV-based data. As shown in Fig. 6(b), the original image exhibited blurred surface features due to
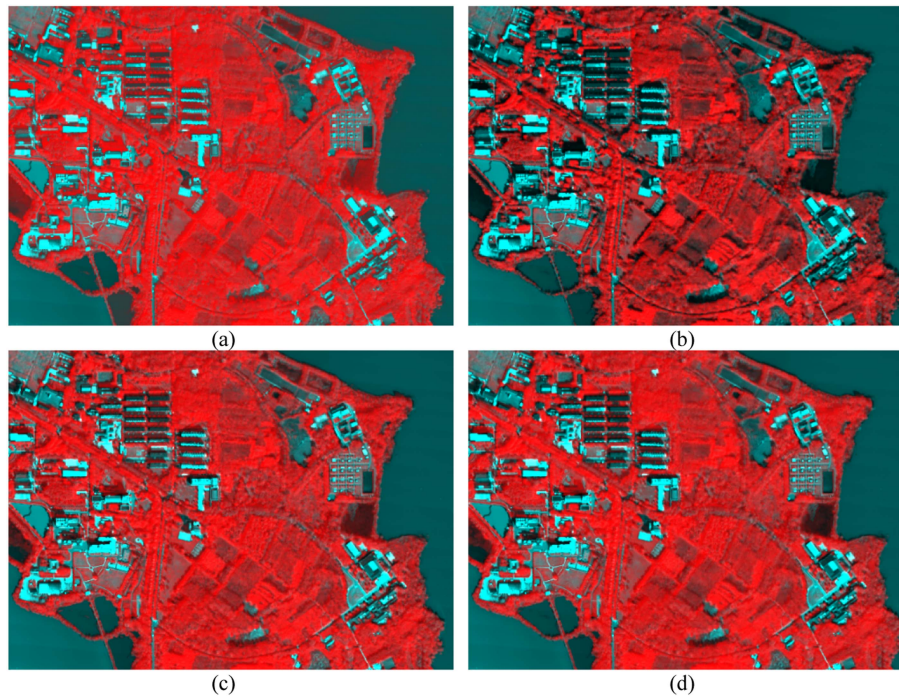
Fig. 7.    RGB composition in false color (R: NDVI; G: UAV-B1; B: UAV-B1;) of NDVI images retrieved from (a) UAV, (b) TOA, (c) Syn-AC, and (d) FLAASH.

TABLE IV
STATISTICS RESULT OF INDICES IMAGE

|  | NDVI | | | NDWI | | |
|---|---|---|---|---|---|---|
|  | Min | Max | Mean | Min | Max | Mean |
| UAV | −0.4561 | 0.9461 | 0.5003 | −1 | 0.6854 | −0.3248 |
| TOA | −0.4712 | 0.6395 | 0.1165 | −0.3611 | 0.7238 | 0.1759 |
| Syn-AC | −0.4818 | 0.8948 | 0.4094 | −0.7867 | 0.7965 | −0.2290 |
| FLAASH | −0.5424 | 0.8917 | 0.3516 | −0.7482 | 0.8241 | −0.1601 |

atmospheric interference. As synchronization atmospheric correction was applied on the satellite data, and the true color image after AC [see Fig. 6(c)] displayed clear edges and rich textures with the removal of the blurring effect. Similarly, the FLAASH method also provided visual enhancement [see Fig. 6(d)].

### B. Retrieval Result of Remote Sensing Indices Images

According to the equations of pixel indices value calculation, the pixel indices values were calculated based on the satellite-derived and UAV-derived reflectance images to produce NDVI and NDWI images (see Figs. 7 and 8). For the purposes of visual comparison, the gray indices images were displayed in the RGB composition in false color, where both G-band and B-band represent the reflectance at band1 of the UAV data, and R-band is the indices value. Table IV shows the statistical results for the pixel values in the NDVI and NDWI images derived from the satellite TOA and BOA reflectance and UAV reflectance. It evident that AC methods yield a greater range of pixel values in the indices images in comparison to TOA. The

UAV-NDVI has the highest upper limit (∼0.95), while that of the TOA-NDVI image was the lowest (∼0.64). In the case of NDWI, the range of pixel value in indices images varies considerably. The maximum pixel value of FLAASH-NDWI was the highest (∼0.82) in contrast to the UAV-NDWI image (∼0.69), followed by Syn-AC-NDWI (∼0.79), and TOA-NDWI (∼0.72). As the NDVI images shown in Fig. 7, the area delineated in red represents the region exhibiting vegetative growth, with the depth of the red hue indicative of the extent of such growth. Thus, it is relatively straightforward to differentiate between vegetation and nonvegetation based on color. It can be observed that certain areas with vegetation coverage, especially the region covered by vegetation around buildings, are labeled in red in the BOA-NDVI images, while the red mark is not particularly prominent in the TOA-NDVI image.

Fig. 8 depicts the NDWI images derived from satellite TOA and BOA reflectance and UAV data in the RGB composition (R: NDWI; G: UAV-B1; B: UAV-B1) in false color. In the TOA-NDWI image, the buildings are represented in red, despite not being water bodies. The BOA-NDWI is displayed in a consistent with the UAV-NDWI in the majority of areas.
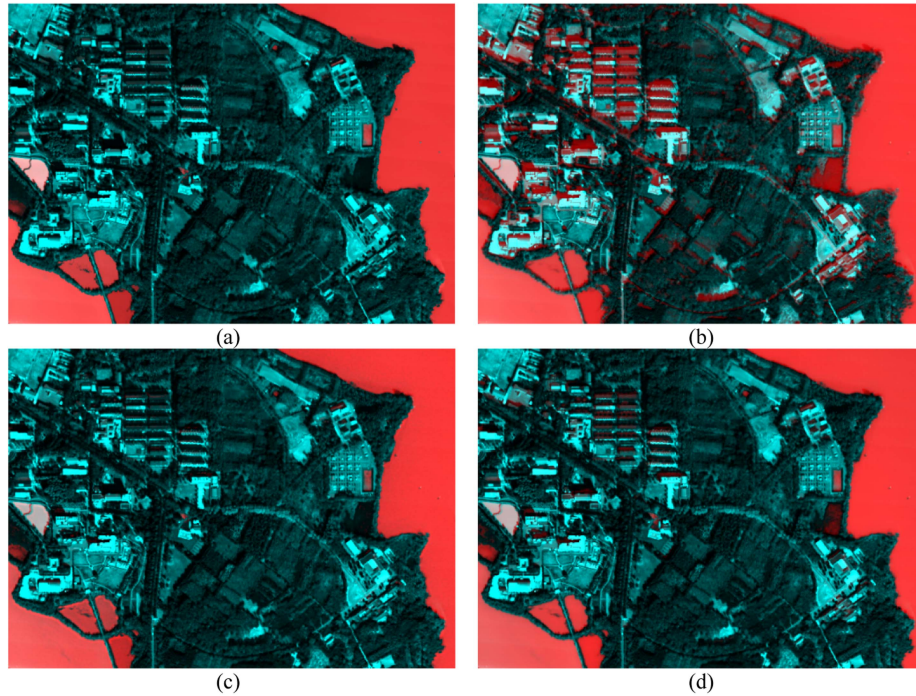
Fig. 8. RGB composition in false color (R: NDWI; G: UAV-B1; B: UAV-B1;) of NDWI images retrieved from (a) UAV, (b) TOA, (c) Syn-AC, and (d) FLAASH.
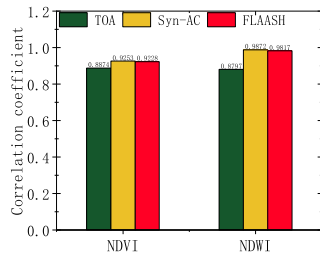


Fig. 9. Correlation between satellite-derived and UAV-derived indices images.
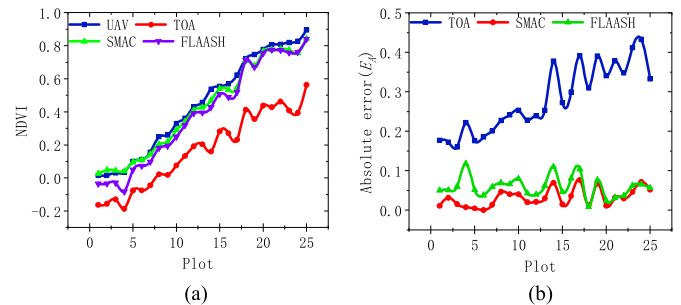


Fig. 10. Results of average NDVI of sampling plots and difference between satellite-derived and UAV-derived values. (a) Average NDVI of sampling plots. (b) Absolute error between satellite-derived and UAV-derived values.

### C. Statistical Analysis

*1) Correlation Between Satellite-Derived and UAV-Derived Indices Images:* According to (21), the NDVI image retrieved from the low-altitude hyperspectral image was used as the reference image, the correlation of the TOA-NDVI and BOA-NDVI images with it were calculated, resulting in coefficient values of 0.8874 (TOA), 0.9253 (Syn-AC), and 0.9228 (FLAASH), respectively. The findings demonstrated that the NDVI images derived from BOA reflectance were more similar to the UAV-NDVI image, in contrast to the TOA-NDVI image. In the case of NDWI, the correlation coefficients between the TOA-NDWI image, the BOA-NDWI images, and the UAV-NDWI image were 0.8797(TOA), 0.9872(Syn-AC), and 0.9817(FLAASH), respectively. It is evident that the BOA-NDWI images after atmospheric correction exhibited greater similarity to the UAV-NDWI image than TOA-NDWI image before atmospheric correction.

*2) Comparison of Average Indices Value of Typical Region:* In this section, the average indices value of the sampling plot in the indices image is investigated. For the NDVI, the mean

values of the selected regions in the NDVI images were obtained and compared [see Fig. 10(a)]. Typical low values of NDVI (lower than 0.2) were observed in asphalt, pavement, and bare soil. In contrast, vegetation-covered plots exhibited a much higher NDVI value, ∼0.8, depending on the AC method. More importantly, the average NDVI values of the sampling plots in BOA-NDVI images after AC demonstrated an increase and were higher in comparison to TOA-NDVI values. Notably, the BOA-NDVI values exhibited a closer alignment with the UAV-NDVI truth values.

Furthermore, the difference in average NDVI of the sampling plot between satellite-derived and UAV-based indices images was also evaluated, and the values are shown in Fig. 10(b). The result indicated that the error between TOA-NDVI with UAV truth value was the most significant, with an overall average error of 0.2807 across all plots. In contrast, the mean error of FLAASH
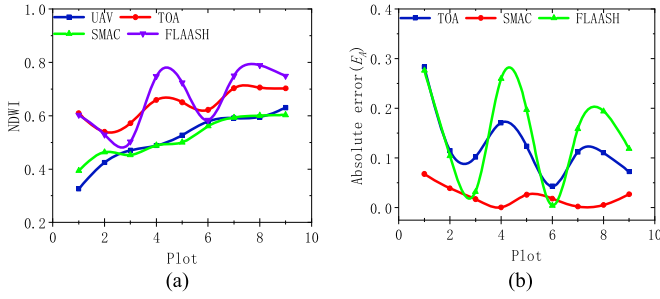
Fig. 11.　Results of average NDWI of sampling plots and difference between satellite-derived and UAV-derived values. (a) Average NDWI of sampling plots. (b) Absolute error between satellite-derived and UAV-derived values.



Fig. 12.　Study regions used for comparison of pixel NDVI value. V1∼V8 are used to label the study regions. (a) V1–V4. (b) V5–V8.

was 0.0593, while that of Syn-AC was 0.0318. Considering the difference of two AC methods, the smallest difference between the NDVI values estimated by Syn-AC and FLAASH was observed in the vegetated area. The greatest difference ($>$0.1) between the AC methods was observed in the artificial surfaces (i.e., pavement and asphalt). According to (24), RMSE between the satellite-derived and the UAV truth results were obtained, with the RMSE results of TOA, FLAASH, and Syn-AC being 0.2928, 0.0645, and 0.0386, respectively. The smallest RMSE value was achieved by synchronization atmospheric correction.

In the case of NDWI, the mean NDWI values of various water bodies were calculated, and the results are presented in Fig. 11(a). It was observed that the average NDWI value of the water bodies ranges from 0.3 to 0.6, and the reason was thought to be that the water quality is different. The mean NDWI value derived from satellite TOA reflectance is considerably higher than the UAV measurements. In contrast to the TOA-NDWI, the Syn-AC method decreased the NDWI inversion results, and as a result that NDWI (Syn-AC) were closer to the UAV values. In the case of FLLASH, the performance varied in different water bodies, with an overestimation of NDWI compared with the UAV truth value. It can be observed that the NDWI (FLAASH) values were lower than the TOA-NDWI in the regions (No. 1, 2, 3, and 6 plots for NDWI in Fig. 1). Conversely, for the remaining plots, FLAASH increased the NDWI compared with the TOA-NDWI values.

Fig. 11(b) shows values in average NDWI of water bodies between satellite-derived and UAV-based results. The absolute error between TOA-NDWI and UAV-NDWI was the maximum for the water bodies (NO. 1, 2, 3, and 6). In contrast, for the remaining plots, the difference between FLAASH -NDWI and UAV-NDWI was the most pronounced. In general, the mean NDWI of each sampling plot after synchronous atmospheric correction is closest to the UAV truth, and the errors of TOA and FLAASH with UAV-NDWI are greater. The average errors compared with UAV-NDWI results are 0.1493 (FLAASH), 0.1258(TOA), and 0.0226(Syn-AC), respectively. Based on the NDWI inversion result, the RMSE of NDWI retrieved from satellite data compared with UAV-NDWI was calculated. The RMSE values are 0.1414(TOA), 0.1735 (FLAASH), and 0.0301(Syn-AC). It was observed that the lowest RMSE value was achieved by synchronous atmospheric correction.
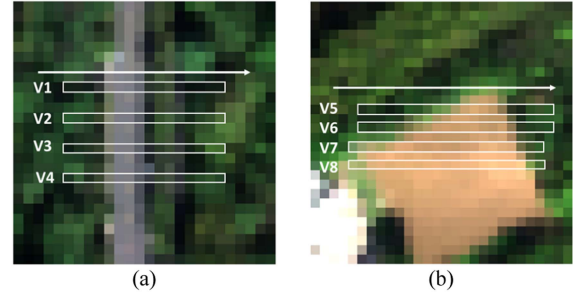
*3) Comparison of Changes in Pixel Indices Value:* Based on the high-resolution NDVI and NDWI images, the values of the indices of pixels in indices images were analyzed. In the case of NDVI, eight tests were conducted. As shown in Fig. 12, the eight rectangles (labeled V1∼V8) represent the study regions, and each one contains some consecutive pixels. Along the arrow direction, the pixels (V1∼V4) are successively covered by vegetation, asphalt pavement and vegetation, and the pixels (V5∼V8) are successively covered by vegetation, bare soil and vegetation. For each test, the NDVI values of consecutive pixels were acquired, and the results are shown in Fig. 13. The findings indicate that both AC methods yield higher BOA-NDVI values compared to TOA-NDVI, and the BOA-NDVI values are closer to UAV-borne results. This aligns with the result regarding the average indices value of the sampling plot. Furthermore, the difference in pixel NDVI values between satellite-derived and UAV-derived results was also calculated, and the values are shown in Fig. 14. The results demonstrate that the difference between TOA-NDVI and UAV-NDVI was the maximum for the majority of pixels. The mean errors for all sampled pixels are 0.2687, 0.0728, and 0.0450 for TOA, FLAASH, and Syn-AC, respectively.

According to (26), the first derivative values of the NDVI values for neighboring pixels within the study areas were calculated and used to evaluate the change of pixel NDVI values. It can be observed that the variation trend of the change rate curve of the NDVI value of pixels in the satellite-derived NDVI images is consistent with that of the UAV-NDVI. As illustrated in Fig. 15, the NDVI change rate in the UAV-NDVI image is used as the reference value, with the two peaks of the change rate curve marked by the vertical lines. It can be seen that the markers align with the boundary points of ground objects as illustrated in Fig. 12. Thus, the peak values of the change rate curves of pixel values retrieved from the satellite-derived and the UAV-derived indices images were investigated. The findings revealed that the change rate value of NDVI for a pixel situated at the boundary of the ground objects is the lowest on the TOA-NDVI image before atmospheric correction. However, postatmospheric correction, the BOA-NDVI exhibited enhanced peak values, aligning more closely with the results of UAV-NDVI. The peak values of the pixel NDVI change rate curves (V1–V8) were analyzed, and the average values of the peak values obtained by UAV, Syn-AC,
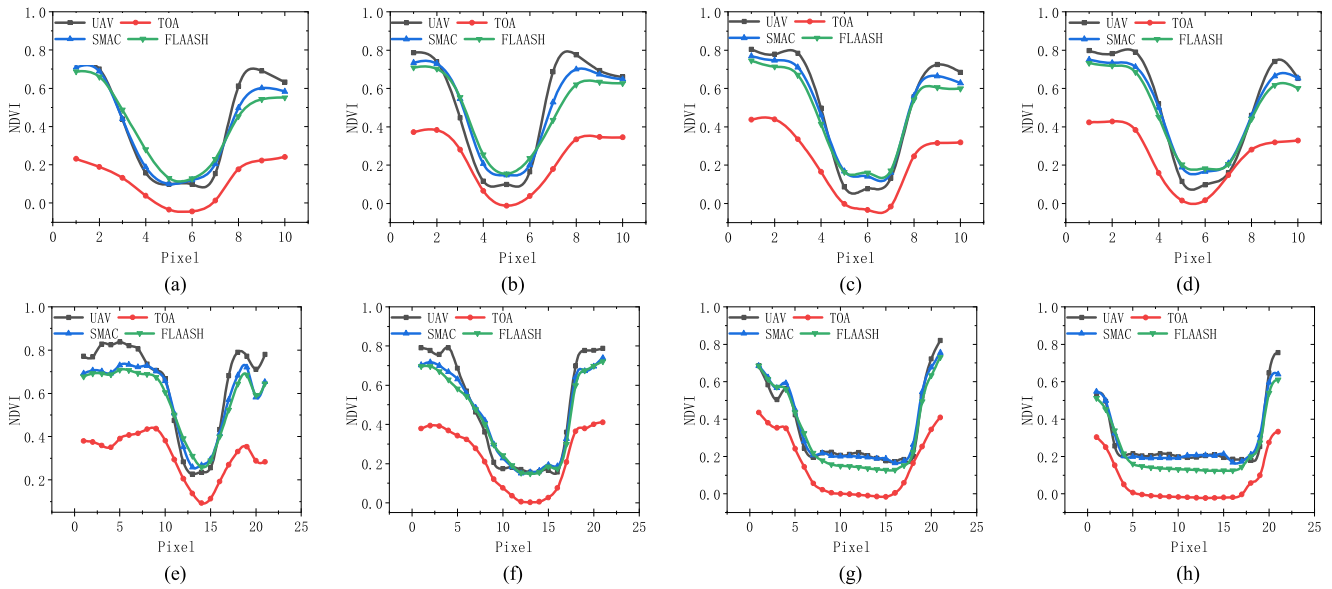
Fig. 13.    NDVI value of pixels in region (a) V1; (b) V2; (c) V3; (d) V4; (e) V5; (f) V6; (g) V7; (h) V8. The $Y$-axis represents the pixel in region.
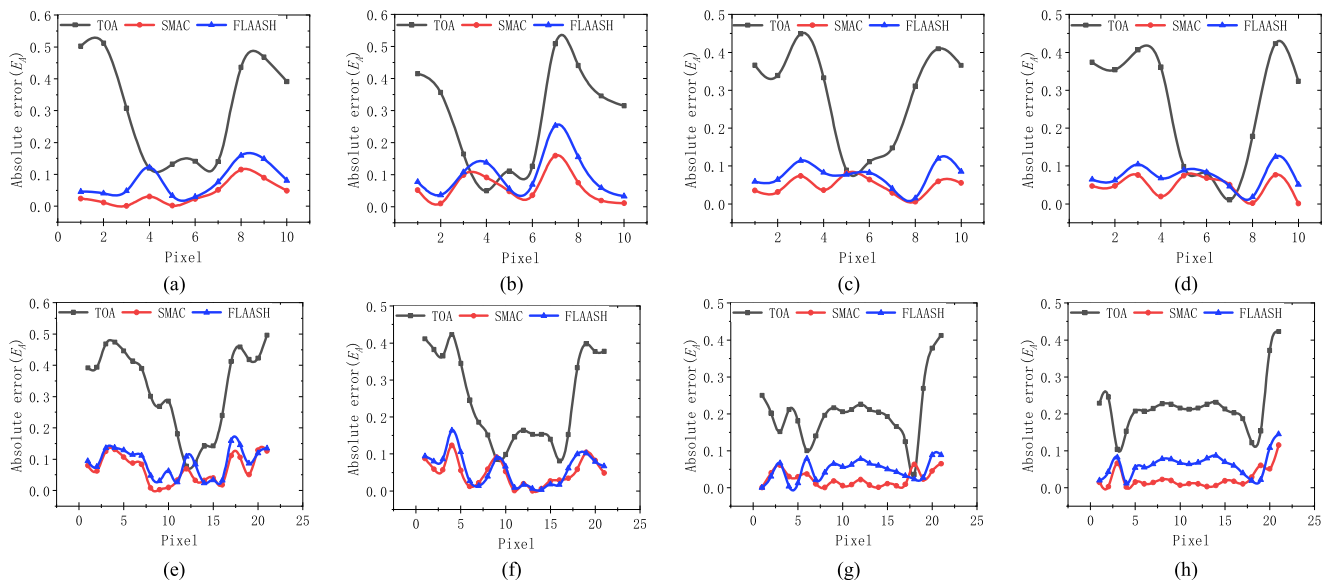


Fig. 14.    Absolute error of pixel value in NDVI images of satellite-derived and UAV-derived (a) V1; (b) V2; (c) V3; (d) V4; (e) V5; (f) V6; (g) V7; (h) V8.

FLAASH, and TOA were 0.3251, 0.2572, 0.2142, and 0.1368, respectively.

Based on the peak values of pixel NDVI change rate curves in the eight study regions, V1–V8, the difference between satellite-derived and UAV-derived peak values was evaluated. Table V presents values in peak value of change rate of NDVI obtained from satellite-derived NDVI images compared with the values of UAV-NDVI image. Notably, the most pronounced difference in peak value was observed between TOA-NDVI and UAV-NDVI, with an average error of all peak values was 0.1883. In contrast, the average error of FLAASH was 0.1109, and that of Syn-AC was 0.0689.

As illustrated in Fig. 16, six regions were selected for the purpose of evaluating the change in pixel NDWI values. The pixel NDWI values of two water bodies and nonwater body targets between them were acquired in each test, and the results are illustrated in Fig. 17. It can be observed that the higher NDWI results were obtained by TOA and FLAASH, especially in the water bodies, but these values were higher than the UAV true values. The pixel NDWI values obtained from the BOA-NDWI image after synchronous atmospheric correction are closer to UAV results. Fig. 18 shows the absolute error in pixel NDWI value between satellite-derived and UAV-derived results. The maximum difference was observed in the case of TOA-NDWI, with an average error of 0.2504. In contrast, the mean error
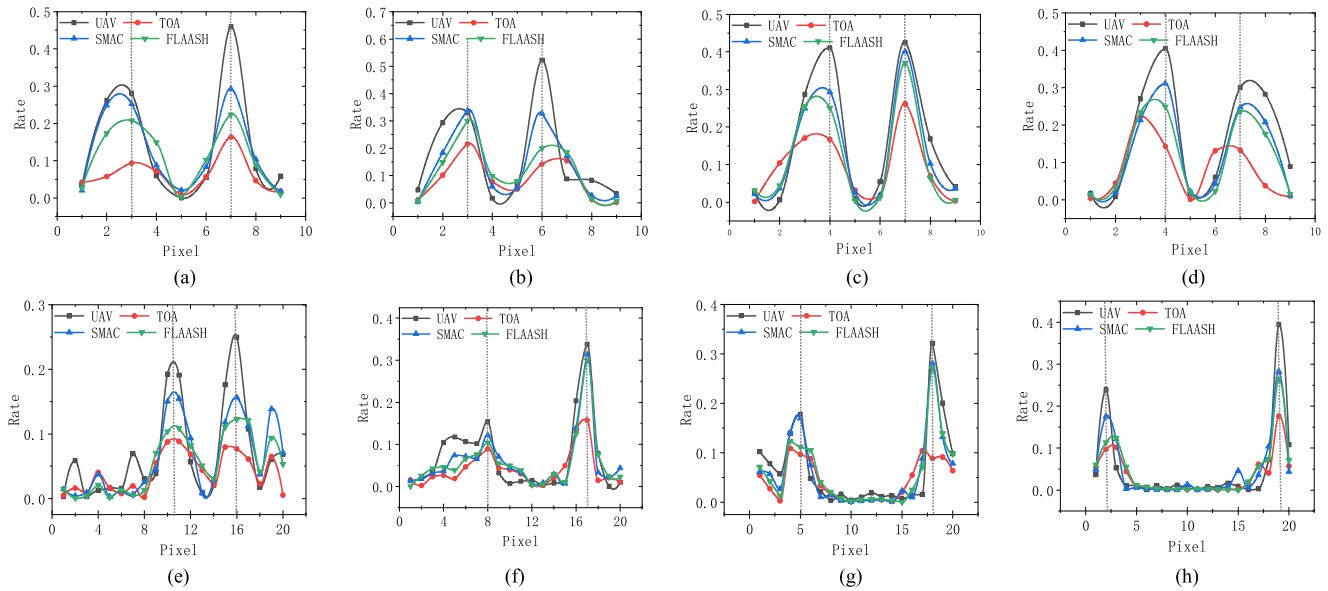
Fig. 15. Change rate in NDVI of pixels in region (a) V1; (b) V2; (c) V3; (d) V4; (e) V5; (f) V6; (g) V7; (h) V8.

TABLE V
ABSOLUTE ERROR OF NDVI CHANGE RATE PEAK BETWEEN SATELLITE-DERIVED AND UAV-DERIVED VALUES

| | | V1 | V2 | V3 | V4 | V5 | V6 | V7 | V8 |
|---|---|---|---|---|---|---|---|---|---|
| | TOA | 0.1880 | 0.1147 | 0.2438 | 0.2625 | 0.1050 | 0.0649 | 0.0804 | 0.1418 |
| Peak 1 | Syn-AC | **0.0291** | **0.0078** | **0.1178** | **0.0939** | **0.0424** | **0.0326** | **0.0078** | **0.0634** |
| | FLAASH | 0.0739 | 0.0301 | 0.1602 | 0.1567 | 0.0887 | 0.0497 | 0.0660 | 0.1256 |
| | TOA | 0.2957 | 0.3811 | 0.1633 | 0.1677 | 0.1726 | 0.1805 | 0.2328 | 0.2180 |
| Peak 2 | Syn-AC | **0.1662** | **0.1957** | **0.0237** | **0.0523** | **0.0931** | **0.0240** | **0.0403** | **0.1118** |
| | FLAASH | 0.2354 | 0.3232 | 0.0551 | 0.0641 | 0.1265 | 0.0382 | 0.0511 | 0.1297 |

The minimum error value is in bold.

in pixel NDWI was 0.0941 for FLAASH, and it is 0.0243 for the Syn-AC method. After AC, the error was notably reduced, particularly through the application of synchronous atmospheric correction.

Subsequently, the change rate of the NDWI value of each pixel in the study area was calculated following the analysis of the pixel NDWI value. The results are depicted in Fig. 19. Meanwhile, the peak change rate values were identified based on the UAV-NDWI imagery. The results demonstrated that the peak values obtained from the TOA-NDWI image consistently exhibited the lowest values compared to those retrieved from the UAV-NDWI image. It is noteworthy that after atmospheric correction, the peak values obtained from the BOA-NDWI images show a considerable improvement. The mean values of all the peak values are 0.4959(UAV), 0.4295(Syn-AC), 0.4035(FLAASH), and 0.1931(TOA). The UAV-derived mean peak value is the highest, followed by Syn-AC and FLAASH, and that in the case of TOA is the lowest in contrast.

The peak values of pixel NDWI change rate curves in the six regions (W1–W6) were analyzed in order to evaluate the difference between satellite-derived and UAV-derived peak values. Table VI presents the absolute errors in the peak value of the change rate of pixel NDWI values obtained from satellite-derived NDWI

images in comparison with those derived from UAV-NDWI images. The results demonstrate that the greatest difference in peak values is observed between TOA-NDVI and UAV-NDVI. Furthermore, the mean peak errors derived from Syn-AC, FLAASH, and TOA were 0.0739, 0.1236, and 0.3028, respectively.

## V. DISCUSSION

In the study, the correlation between satellite-derived and UAV-derived indices images was investigated. The results demonstrated that atmospheric correction has the potential to markedly improve the precision of remote sensing indices images. The correlation coefficients of the NDVI and NDWI images after synchronous atmospheric correction with the UAV-derived results are increased by 4.27% and 12.22%, respectively, in comparison with the indices images retrieved from the satellite TOA reflectance. For FLAASH, the correlation improvements are 3.99% and 11.59% in the case of NDVI and NDWI, respectively. It can be observed that the correlation enhancement of the indices image by the two AC methods is similar, with synchronous atmospheric correction demonstrating a superior performance.

TABLE VI
ABSOLUTE ERROR OF NDWI CHANGE RATE PEAK BETWEEN SATELLITE-DERIVED AND UAV-DERIVED VALUES

|  |  | W1 | W2 | W3 | W4 | W5 | W6 |
|---|---|---|---|---|---|---|---|
|  | TOA | 0.1660 | 0.0909 | 0.4850 | 0.4981 | 0.1475 | 0.4934 |
| Peak 1 | Syn-AC | **0.0017** | **0.0148** | 0.1439 | **0.0132** | 0.0515 | **0.1368** |
|  | FLAASH | 0.0099 | 0.1159 | **0.1261** | 0.0616 | **0.0329** | 0.2393 |
|  | TOA | 0.2222 | 0.2642 | 0.3655 | 0.4195 | 0.1972 | 0.2838 |
| Peak 2 | Syn-AC | **0.0154** | **0.1886** | **0.1445** | 0.0804 | **0.0541** | **0.0420** |
|  | FLAASH | 0.0766 | 0.2376 | 0.2543 | **0.0763** | 0.0900 | 0.1630 |

The minimum error value is in bold.
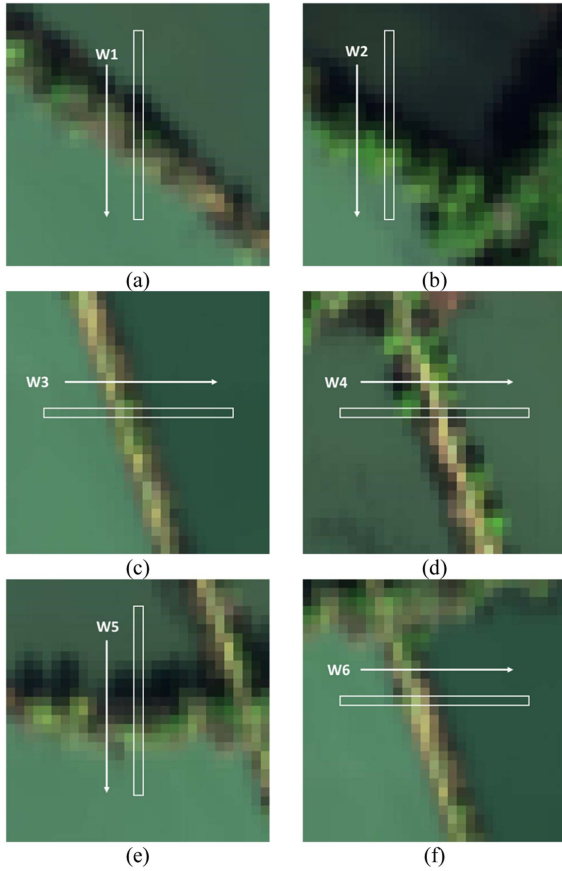


Fig. 16. Study regions used for comparison of pixel NDWI value. W1–W6 are used to label the study regions. (a) W1. (b) W2. (c) W3. (d) W4. (e) W5. (f) W6.

Moreover, a number of typical regions were selected as sampling plots, and the mean indices values for each plots were obtained. Subsequently, the average indices values of the plots obtained from satellite-derived indices images were compared with those derived from the low-altitude indices images. The results demonstrate that the average NDVI value of each sampling plot after atmospheric correction exhibits an improvement, approximating the average value observed in the corresponding region within the low-altitude indices image. Consequently, the inversion error subsequent to AC is diminished (as illustrated in Fig. 10). The mean error of the NDVI in all sampling plots was calculated, and the mean error of the NDVI after Syn-AC

and FLAASH methods was reduced by 0.2489 and 0.2214, respectively. The two AC methods have comparable effects on improving the precision of the average NDVI of the sampling plot. In addition, the RMSE values indicate that the error variability after synchronous atmospheric correction is less than that of FLAASH, exhibiting a more stable performance of indices inversion.

In the case of the average NDWI of water body, the performance of Syn-AC differs from that of FLAASH. In contrast to TOA-NDWI, the average error between NDWI after Syn-AC and UAV-NDWI decreased by 0.1032. However, the average error of NDWI after FLLASH increased by 0.0235. The reason was thought to be that the water body is a ground object with low reflectance, and that the contribution of atmospheric radiation occupies the majority part of the detection signal of the remote sensing sensor. Especially in the NIR band involved in NDWI calculation, it is generally considered that the signal emitted by the water body within this band is, in essence, an atmospheric radiation signal (such as the darkest-pixel method). It is essential that the atmospheric parameters are synchronized in terms of both time and space scales with the remote sensing image that is to be corrected, in order to ensure the accurate removal of atmospheric radiation interference. FLAASH is an atmospheric correction method based on empirical parameters, which is unable to accurately remove the atmospheric radiation interference. As illustrated in Fig. 11, the error of the average NDWI of the sampling plot after the correction by FLAASH is higher overall, and the error fluctuation is larger than that of Syn-AC. FLAASH exhibited superior performance in some plots, such as NDWI plots No. 3 and No. 6 for NDWI (depicted in Fig. 1).

In the process of high-resolution remote sensing imaging, the atmospheric adjacent effect must be taken into account. In the paper, the areas that contain two different ground objects were selected as study regions to investigate the changes in the indices value of pixels in the boundary of the different ground objects in the NDVI and NDWI images. The results demonstrate that the atmospheric adjacent effect affects the inversion accuracy of remote sensing indices, resulting in the blurring of the surface feature types at the boundary.

The spatial variation trend of the indices value of pixels in the boundary is not consistent with the UAV-derived reference result, as evidenced by the indices image retrieved from the satellite TOA reflectance. In comparison to the results obtained from UAV-derived indices images, the average error in NDVI value
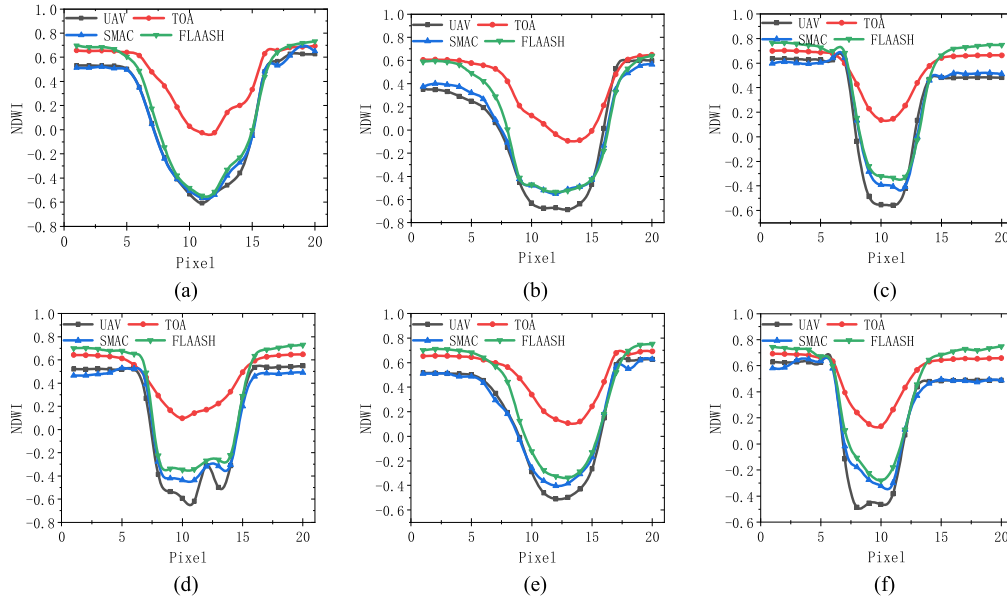
Fig. 17.    NDWI value of pixels in region (a) W1; (b) W2; (c) W3; (d) W4; (e) W5; (f) W6. The *Y*-axis represents the pixel in region.
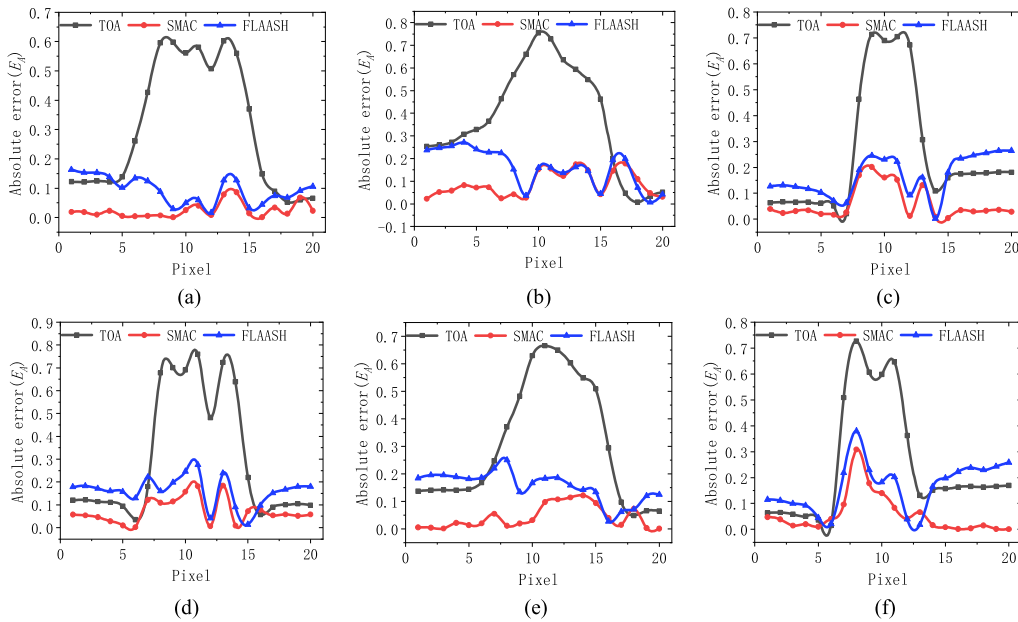


Fig. 18.    Absolute error of pixel value in NDWI images of satellite-derived and UAV-derived (a) W1; (b) W2; (c) W3; (d) W4; (e) W5; (f) W6.

of pixels situated within the "vegetation—ground—vegetation" regions in the satellite-derived indices images obtained by TOA, FLAASH, and Syn-AC are 0.2687, 0.0728, and 0.0450, respectively. The two AC methods yield comparable effects in terms of improving the inversion accuracy of pixel NDVI value, with a decrease in mean error of 0.2238 (Syn-AC) and 0.1960(FLAASH). On the other hand, the peak values of pixel NDVI change rate curves obtained from UAV-NDVI are the highest, reflecting the real surface type changes. In comparison with the peak value of the pixel NDVI change rate in the UAV-NDVI image, the mean error in peak values for TOA, FLAASH,

and Syn-AC are 0.1883, 0.1109, and 0.0689, respectively. The lowest discrepancy was observed in the case of synchronous atmospheric correction, with a decrease in mean peak error of 0.1194 in comparison with that of TOA-NDVI.

In the case of the NDWI values of pixels in the "water—ground—water" regions, the mean error values in pixel NDWI retrieved from satellite-derived images are 0.2504 (TOA), 0.0941 (FLAASH), and 0.0243 (Syn-AC), respectively. The best performance was observed in Syn-AC, with a significant reduction of 0.2260 in mean error. Meanwhile, compared with the peak values of pixel NDWI change rate in the UAV-NDWI
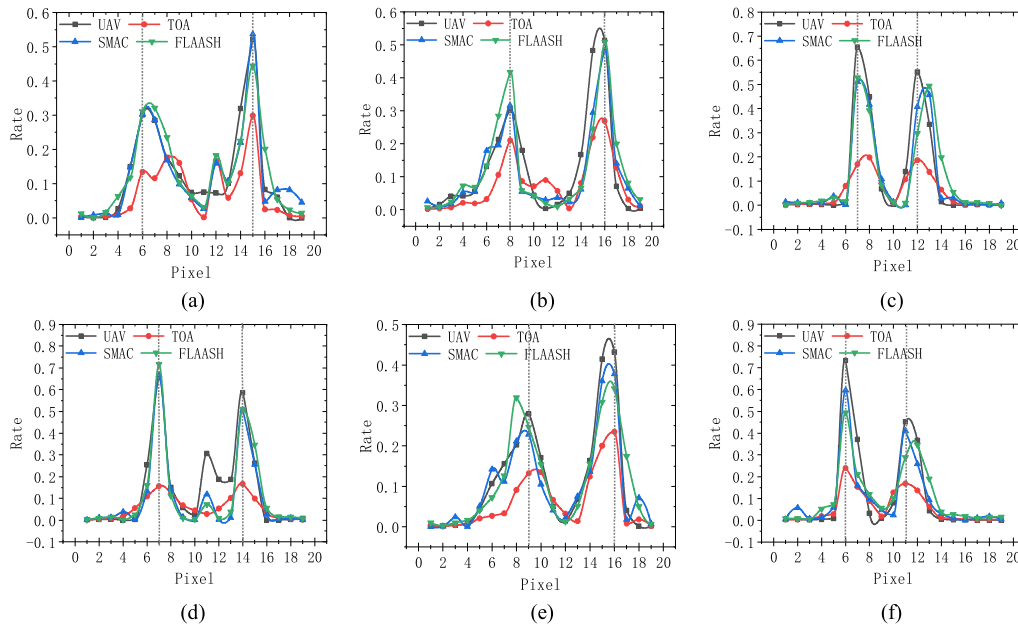
Fig. 19.    Change rate in NDWI of pixels in regions (a) W1; (b) W2; (c) W3; (d) W4; (e) W5; (f) W6.

image, the mean error in peak value for TOA, FLAASH, and Syn-AC are 0.3028, 0.1236, and 0.0739, respectively. The Syn-AC method yields the most accurate results with the lowest error, and a decrease of 0.2288 in mean peak error was observed. Consequently, the performance of the synchronous atmospheric correction method for the correction of adjacent effect is generally superior to than that of FLAASH.

## VI. CONCLUSION

To investigate the effect of synchronous atmospheric correction on the inversion accuracy of high-resolution remote sensing indices images, the "spaceborne—(low altitude) airborne" synchronous imaging experiment was designed and conducted to compare the accuracy of the remote sensing indices images obtained from the GFDM multispectral images before and after the synchronous atmospheric correction method which is based on the atmospheric parameters retrieved from the synchronization monitoring atmospheric corrector equipment. Meanwhile, the performance of synchronous atmospheric correction is compared with that of a nonsynchronous correction method, FLAASH. The experiment results demonstrate that the remote sensing indices images after atmospheric correction are significantly improved in terms of spatial distribution, numerical accuracy, and spatial variation trend of the pixel index value. Additionally, the synchronous atmospheric correction shows better performance than the classical nonsynchronous correction method.

As the commonly used remote sensing indices, NDVI and NDWI, on which many other remote sensing indices are further retrieved, play an important fundamental role in extraction of surface information. It is observed that the difference of 0.05 in NDVI can produce 30% of the grassland yield estimation error in the study of Kaufman and Tanre [2]. Liu et

al. [8] found that the coefficient of determination of NDWI for winter wheat yield estimate was 0.79. Applying of atmospheric correction to improve the accuracy of remote sensing indices has great influence on the quantitative applications of remote sensing information. Compared with the classical atmospheric correction method, FLAASH, the Syn-AC method proposed in this article has a more obvious effect on improving the accuracy of remote sensing indices in the low-reflectance targets with a higher proportion of atmospheric radiation contribution, and in the boundary regions of different ground objects. Therefore, for the extraction of low-reflectivity ground object information and its application, such as water quality detection, wetland monitoring, etc., especially for applications that rely on high-resolution remote sensing information, such as the health monitoring of single economic crop and the yield prediction, synchronous atmospheric correction provides an important guarantee for the accuracy of surface information extraction.

Through the experiment and the comparative analysis of the experimental results, the preliminary conclusion of the effect of synchronous atmospheric correction method on the remote sensing indices error is formed. In addition, there are still some issues that need further investigations. For example, under the impact of different atmospheric conditions, the effect of synchronous atmospheric correction on the accuracy of other remote sensing indices, especially the effect of adjacent effect correction on the pixel-level indices accuracy, needs to be further analyzed by targeted experiments.

## REFERENCES

[1] Z. Zhang et al., "Stand density estimation based on fractional vegetation coverage from Sentinel-2 satellite imagery," *Int. J. Appl. Earth Observ. Geoinf.*, vol. 108, 2022, Art. no. 102760, doi: 10.1016/j.jag.2022.102760.

[2] Y. J. Kaufman and D. Tanre, "Atmospherically resistant vegetation index (ARVI) for EOS-MODIS," *IEEE Trans. Geosci. Remote Sens.*, vol. 30, no. 2, pp. 261–270, Mar. 1992, doi: 10.1109/36.134076.

[3] O. Lfgren et al., "Landscape history confounds the ability of the NDVI to detect fine-scale variation in grassland communities," *Methods Ecol. Evol.*, vol. 9, pp. 2009–2018, 2018, doi: 10.1111/2041-210X.13036.

[4] J. T. Compton, "Red and photographic infrared linear combinations for monitoring vegetation," *Remote Sens. Environ.*, vol. 8, no. 2, pp. 127–150, 1979.

[5] Y. Kang et al., "How universal is the relationship between remotely sensed vegetation indices and crop leaf area index? A global assessment," *Remote Sens.*, vol. 8, no. 7, pp. 597, 2016.

[6] R. S. DeFries and J. R. G. Townshend, "NDVI-derived land cover classifications at a global scale," *Int. J. Remote Sens.*, vol. 15, no. 17, pp. 3567–3586, 1994.

[7] R. S. Lunetta et al., "Land-cover change detection using multi-temporal MODIS NDVI data," *Remote Sens. Environ.*, vol. 105, pp. 142–154, 2006.

[8] J. Liu et al., "Winter wheat yield estimation method based on NDWI and convolutional neural network," *Trans. Chin. Soc. Agricultural Machinery*, vol. 52, no. 12, pp. 273–280, 2021.

[9] S. Vanonckelen, S. Lhermitte, and A. Van Rompaey, "The effect of atmospheric and topographic correction methods on land cover classification accuracy," *Int. J. Appl. Earth Observ. Geoinf.*, vol. 24, no. 1, pp. 9–21, 2013, doi: 10.1016/j.jag.2013.02.003.

[10] C. K. Min et al., "Landslide assessment using normalized difference vegetation index (NDVI)," *J. Trop. Resour. Sustain. Sci.*, vol. 4, pp. 98–104, 2016, doi: 10.47253/j-trss.v4i2.615.

[11] S. Xu et al., "The damage of urban vegetation from super typhoon is associated with landscape factors: Evidence from Sentinel-2 imagery," *Int. J. Appl. Earth Observ. Geoinf.*, vol. 104, 2021, Art. no. 102536, doi: 10.1016/j.jag.2021.102536.

[12] M. A. Friedl et al., "Scaling and uncertainty in the relationship between the NDVI and land surface biophysical variables: An analysis using a scene simulation model and data from FIFE," *Remote Sens. Environ.*, vol. 54, no. 3, pp. 233–246, 1995, doi: 10.1016/0034-4257(95)00156-5.

[13] P. Fu and Q. Weng, "A time series analysis of urbanization induced land use and land cover change and its impact on land surface temperature with Landsat imagery," *Remote Sens. Environ.*, vol. 175, pp. 205–214, 2016, doi: 10.1016/j.rse.2015.12.040.

[14] M. Gilabert et al., "A generalized soil adjusted vegetation index," *Remote Sens. Environ.*, vol. 82, no. 2, pp. 303–310, 2002, doi: 10.1016/S0034-4257 (02)00048-2.

[15] Z. Zhen et al., "Globally quantitative analysis of theimpact of atmosphere and spectral response function on 2-band enhanced vegetation index (EVI2) over Sentinel-2 and Landsat-8," *ISPRS J. Photogrammetry Remote Sens.*, vol. 205, pp. 206–226, 2023, doi: 10.1016/j.isprsjprs.2023.09.024.

[16] D. Moravec et al., "Effect of atmospheric corrections on NDVI: Intercomparability of Landsat 8, Sentinel-2, and UAV sensors," *Remote Sens.*, vol. 13, 2021, Art. no. 3550, doi: 10.3390/rs13183550.

[17] P. M. Teillet, "Image correction for radiometric effects in remote sensing," *Int. J. Remote Sens.*, vol. 7, pp. 1637–1651, 1986.

[18] O. Hagolle et al., "A multi-temporal and multi-spectral method to estimate aerosol optical thickness over land, for the atmospheric correction of FormoSat-2, LandSat, VEN$\mu$S and Sentinel-2 images," *Remote Sens.*, vol. 7, no. 3, pp. 2668–2668, 2015, doi: 10.3390/rs70302668.

[19] X. Xiong et al., "Updates of moderate resolution imaging spectroradiometer on-orbit calibration uncertainty assessments," *J. Appl. Remote Sens.*, vol. 12, no. 3, 2018, Art. no. 034001, doi: 10.1117/1.JRS.12.034001.

[20] C. Revel et al., "Results from the radiometric absolute calibration of Sentinel-2A and Sentinel-2B," in *Proc. Conf. Characterization Radiometric Calibration Remote Sens.*, 2017.

[21] D. Courault, B. Seguin, and A. Olioso, "Review to estimate evapotranspiration from remote sensing data: Some examples from the simplified relationship to the use of mesoscale atmospheric models," in *Proc. ICID Workshop Remote Sens. ET Large Regions*, 2003, vol. 17, pp. 1–18.

[22] N. Che and J. C. Price, "Survey of radiometric calibration results and methods for visible and near infrared channels of NOAA-7,-9, and -11 AVHRRs," *Remote Sens. Environ.*, vol. 41, pp. 19–27, 1992, doi: 10.1016/0034-4257(92)90057-Q.

[23] C. Song and C. E. Woodcock, "Monitoring forest succession with multitemporal Landsat images: Factors of uncertainty," *IEEE Trans. Geosci. Remote Sens.*, vol. 41, no. 11, pp. 2557–2567, Nov. 2003.

[24] K. Tachiiri, "Calculating NDVI for NOAA/AVHRR data after atmospheric correction for extensive images using 6S code: A case study in the Marsabit district, Kenya," *ISPRS J. Photogrammetry Remote Sens.*, vol. 59, no. 3, pp. 103–114, 2005, doi: 10.1016/j.isprsjprs.2004.09.001.

[25] D. G. Hadjimitsis et al., "Atmospheric correction for satellite remotely sensed data intended for agricultural applications: Impact on vegetation indices," *Natural Hazards Earth Syst. Sci.*, vol. 10, no. 1, pp. 89–95, 2010, doi: 10.5194/nhess-10-89-2010.

[26] G. Guyot and X. F. Gu, "Effect of radiometric corrections on NDVI-determined from SPOT-HRV and Landsat-TM data," *Remote Sens. Environ.*, vol. 49, no. 3, pp. 169–180, 1994, doi: 10.1016/0034-4257 (94)90012-4.

[27] Y. Xie, X. Zhao, L. Li, and H. Wang, "Calculating NDVI for Landsat7-ETM data after atmospheric correction using 6S model: A case study in Zhangye city, China," in *Proc. 18th Int. Conf. Geoinf.*, 2010, pp. 1–4, doi: 10.1109/GEOINFORMATICS.2010.5567553.

[28] X.-M. Zhu, X.-N. Song, P. Leng, D. Guo, and S.-H. Cai, "Impact of atmospheric correction on spatial heterogeneity relations between land surface temperature and biophysical compositions," *IEEE Trans. Geosci. Remote Sens.*, vol. 59, no. 3, pp. 2680–2697, Mar. 2021.

[29] Q. Jiao et al., "Atmospherically resistant vegetation water indices using the 970-nm water absorption feature," *J. Appl. Remote Sens.*, vol. 14, no. 3, 2020, Art. no. 034504.

[30] L. weigang et al., "Variation of FY-A/MERSI data after atmospheric correction based on FLAASH model," *Plateau Meteorolory*, vol. 32, no. 4, pp. 1140–1147, 2013.

[31] W. Ma et al., "An automatic morphological attribute building extraction approach for satellite high spatial resolution imagery," *Remote Sens.*, vol. 11, no. 3, p. 337, 2019.

[32] L. F. Zhang et al., "Calculation of the terrestrial vegetation index VI-UPD using MODIS," *Geomatics Inf. Sci. Wuhan Univ.*, vol. 30, no. 8, pp. 699–702, 2005.

[33] F. Chen et al., "Open water detection in urban environments using high spatial resolution remote sensing imagery," *Remote Sens. Environ.*, vol. 242, 2020, Art. no. 111706.

[34] Z. Y. Avdan et al., "Monitoring the water quality of small water bodies using high-resolution remote sensing data," *ISPRS Int. J. Geo-Inf.*, vol. 8, no. 12, p. 553, 2019.

[35] X. Huang and L. Zhang, "A Multidirectional and multiscale morphological index for automatic building extraction from multispectral GeoEye-1 imagery," *Photogrammetric Eng. Remote Sens.*, vol. 77, pp. 721–732, 2011, doi: 10.14358/PERS.77.7.721.

[36] P. S. Chavez Jr., "An improved dark-object subtraction technique for atmospheric scattering correction of multispectral data," *Remote Sens. Environ.*, vol. 24, no. 3, pp. 459–479, 1988.

[37] P. S. Chavez Jr., "Radiometric calibration of Landsat thematic mapper multispectral images," *Photogrammetric Eng. Remote Sens.*, vol. 55, no. 9, pp. 1285–1294, 1989.

[38] P. S. Chavez, "Image-based atmospheric corrections-revisited and improved," *Photogrammetric Eng. Remote Sens.*, vol. 62, no. 9, pp. 1025–1035, 1996.

[39] B. Alexander, L. S. Bernstein, and D. C. Robertson, "MODTRAN: A moderate resolution model for LOWTRAN 7, 1989.

[40] J. F. De Haan et al., "Removal of atmospheric influences on satellite-borne imagery: A radiative transfer approach," *Remote Sens. Environ.*, vol. 37, no. 1, pp. 1–21, 1991.

[41] E. F. Vermote et al., *Second Simulation of the Satellite Signal in the Solar Spectrum (6S), 6S User's Guide Version 2*. Greenbelt, MD, USA: NASA Goddard Space Flight Center, 1997.

[42] Y. D. Hu et al., "Polarization atmospheric corrector with dual angle for remote sensing image," *Opt. Precis. Eng.*, vol. 23, pp. 652–659, 2015.

[43] R. G. Holm et al., "Surface reflectance factor retrieval from thematic mapper data," *Remote Sens. Environ.*, vol. 27, no. 1, pp. 47–57, 1989.

[44] M. S. Moran et al., "Evaluation of simplified procedures for retrieval of land surface reflectance factors from satellite sensor output," *Remote Sens. Environ.*, vol. 41, no. 2/3, pp. 169–184, 1992.

[45] Z. Li et al., "Preliminary on-orbit performance test of the first polarimetric synchronization monitoring atmospheric corrector (SMAC) on-board high-spatial resolution satellite Gao Fen Duo Mo (GFDM)," *IEEE Trans. Geosci. Remote Sens.*, vol. 60, 2022, Art. no. 4104014, doi: 10.1109/TGRS.2021.3110320.

[46] X. Tang et al., "Adjacency effect correction of GF-1 satellite multispectral remote sensing images," *Acta Optica Sin.*, vol. 36, 2016, Art. no. 0228003.

[47] T. Wang et al., "An adaptive atmospheric correction algorithm for the effective adjacency effect correction of submeter-scale spatial resolution optical satellite images: Application to a WorldView-3 panchromatic image," *Remote Sens. Environ.*, vol. 259, 2021, Art. no. 112412.

[48] L. J. Fan et al., "Scheme design and technical characteristics of high-resolution multimode satellite," *Spacecraft Eng.*, vol. 30, pp. 10–19, 2021.

[49] W. Jiang and Q. L. Huang, "The high-resolution multimode Integrated Imaging satellite was successfully launched. Spacefly," *Return Remote Sens.*, vol. 41, p. 2, 2020.

[50] L. Xu et al., "Synchronous atmospheric correction of high spatial resolution images from Gao Fen Duo Mo satellite," *Remote Sens.*, vol. 14, 2022, Art. no. 4427, doi: 10.3390/rs14174427.

[51] Q. Kang et al., "Experimental study on filter screening method and accuracy verification of atmospheric synchronous corrector," *Acta Optica Sin.*, vol. 37, 2017, Art. no. s11.

[52] R. C. Levy et al., "Global evaluation of the collection 5 MODIS dark-target aerosol products over land," *Atmos. Chem. Phys.*, vol. 10, no. 21, pp. 10399–10420, 2010, doi: 10.5194/acp-10-10399-2010.

[53] P. Ciren and S. Kondragunta, "Dust aerosol index (DAI) algorithm for MODIS," *J. Geophys. Res. Atmos.*, vol. 119, pp. 4770–4792, 2014.

[54] D. K. Hall, G. A. Riggs, and V. V. Salomonson, "Development of methods for mapping global snow cover using moderate resolution imaging spectroradiometer data," *Remote Sens. Environ.*, vol. 54, pp. 127–140, 1995, doi: 10.1016/0034-4257 (95)00137-P.

[55] F. Zheng et al., "Aerosol retrieval study from multiangle polarimetric satellite data based on optimal estimation method," *J. Appl. Remote Sens.*, vol. 14, no. 1, 2020, Art. no. 014516, doi: 10.1117/1.JRS.14.014516.

[56] F. Waquet et al., "Analysis of the spectral and angular response of the vegetated surface polarization for the purpose of aerosol remote sensing over land," *Appl. Opt.*, vol. 48, no. 6, pp. 1228–1228, 2009, doi: 10.1364/ao.48.001228.

[57] P. Litvinov, O. Hasekamp, and B. Cairns, "Models for surface reflection of radiance and polarized radiance: Comparison with airborne multi-angle photopolarimetric measurements and implications for modeling top-of-atmosphere measurements," *Remote Sens. Environ.*, vol. 115, no. 2, pp. 781–792, 2011.

[58] J. Wang et al., "A numerical testbed for remote sensing of aerosols, and its demonstration for evaluating retrieval synergy from a geostationary satellite constellation of GEO-CAPE and GOES-R," *J. Quantitative Spectrosc. Radiative Transfer*, vol. 146, pp. 510–528, 2014.

[59] O. Dubovik et al., "Statistically optimized inversion algorithm for enhanced retrieval of aerosol properties from spectral multi-angle olarimetric satellite observations," *Atmos. Meas. Techn.*, vol. 4, pp. 975–1018, 2011, doi: 10.5194/amtd-3-4967-2010.

[60] E. F. Vermote and S. Kotchenova, "Atmospheric correction for the monitoring of land surfaces," *J. Geophysical Res.: Atmos.*, vol. 113, no. D23, 2008, doi: 10.1029/2007JD009662.

[61] R. Bennartz and J. Fischer, "Retrieval of columnar water vapour over land from backscattered solar radiation using the medium resolution imaging spectrometer," *Remote Sens. Environ.*, vol. 78, pp. 274–283, 2001, doi: 10.1016/S0034-4257 (01)00218-8.

[62] S. Bouffies et al., "Atmospheric water vapor estimate by a differential absorption technique with the POLDER instrument," *Int. Soc. Opt. Photon.*, vol. 2582, pp. 131–143, 1995, doi: 10.1117/12.228543.

[63] C. J. Tucker et al., "Satellite remote sensing of total herbaceous biomass production in the senegalese sahel: 1980–1984," *Remote Sens. Environ.*, vol. 17, pp. 233–249, 1985.

[64] S. K. McFeeters, "The use of the normalized difference water index (NDWI) in the delineation of open water features," *Int. J. Remote Sens.*, vol. 17, no. 7, pp. 1425–1432, 1996.

[65] M. Jianwen, L. Xiaowen, C. Xue, and F. Chun, "Target adjacency effect estimation using ground spectrum measurement and Landsat-5 satellite data," *IEEE Trans. Geosci. Remote Sens.*, vol. 44, no. 3, pp. 729–735, Mar. 2006, doi: 10.1109/tgrs.2005.861545.

[66] M. Xiaoshan et al., "Simulation and analysis of the adjacency effect in earth-imaging process of the optical remote sensing," *J. Infrared Millimeter Waves*, vol. 34, no. 2, pp. 250–256, 2015, doi: 10.11972/j.issn.1001-9014.2015.02.021.

[67] Y. J. Kaufman, "The atmospheric effecton remote sensing and its correction," *Theory Appl. Opt. Remote Sens.*, 1989.

[68] S. Adler-Golden et al., *FLAASH, a Modtran4 Atmospheric Correction Package for Hyperspectral Data Retrievals and Simulations*. Pasadena, CA, USA: JPL, 1998.

[69] *FLAASH User's Guide; ENVI FLAASH Version 1.0*. Norwalk, CT, USA: Res. Syst., 2001, pp. 8–40.

**Lingling Xu** is currently working toward the Ph.D. degree in electronics and information at the University of Science and Technology of China, Hefei, China.

Her research interests include atmospheric correction of optical remote sensing images and quantitative application of remote sensing.
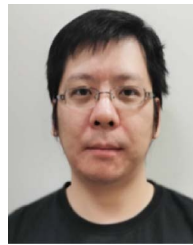
**Wei Xiong** received the Ph.D. degree in optics from the Anhui Institute of Optics and Fine Mechanics, Chinese Academy of Sciences (CAS), Hefei, China, in 2007.

He is currently a Professor with the Optical Remote Sensing Research Center, Anhui Institute of Optics and Fine Mechanics, Hefei Institutes of Physical Science, CAS. He is involved into and completed more than 20 national key projects such as Innovation Fund of Chinese Academy of Sciences, National Natural Science Foundation, 863 Program, and national major projects, authored and coauthored more than 50 papers and more than 10 patents. His research interests include hyperspectral remote sensing technology research.

**Weining Yi** received the B.S. degree in mathematics from Anhui University, Hefei, China, in 1982.

She is currently a Professor with the Optical Remote Sensing Research Center, Anhui Institute of Optics and Fine Mechanics, Hefei Institutes of Physical Science, Chinese Academy of Sciences, Hefei. Her research interests include remote sensing digital image processing and remote sensing information analysis and processing.

**Wenyu Cui** received the Ph.D. degree in optics from the Anhui Institute of Optics and Fine Mechanics, Chinese Academy of Sciences (CAS), Hefei, China, in 2013.

He is currently an Associate Professor with the Optical Remote Sensing Research Center, Anhui Institute of Optics and Fine Mechanics, Hefei Institutes of Physical Science, CAS. His research interests include remote sensing mechanism and remote sensing information representation.

**Xiao Liu** received the Ph.D. degree in optics from the Anhui Institute of Optics and Fine Mechanics, Chinese Academy of Sciences (CAS), Hefei, China, in 2013.

He is currently an Associate Professor with Optical Remote Sensing Research Center, Anhui Institute of Optics and Fine Mechanics, Hefei Institutes of Physical Science, CAS. His research interests include quantitative optical remote sensing and polarization optical measurement.

**Yuyao Wang** is currently working toward the Ph.D. degree in optics at the University of Science and Technology of China, Hefei, China.

Her research interests include atmospheric optical remote sensing and atmospheric disturbance density field detection.